Uncertainty Analysis and Order-by-Order Optimization of Chiral Nuclear Interactions

B. D. Carlsson,[1,*] A. Ekström,[2,3,†] C. Forssén,[1,2,3,‡] D. Fahlin Strömberg,[1] G. R. Jansen,[3,4] O. Lilja,[1] M. Lindby,[1] B. A. Mattsson,[1] and K. A. Wendt[2,3]

[1]*Department of Physics, Chalmers University of Technology, SE-412 96 Göteborg, Sweden*
[2]*Department of Physics and Astronomy, University of Tennessee, Knoxville, Tennessee 37996, USA*
[3]*Physics Division, Oak Ridge National Laboratory, Oak Ridge, Tennessee 37831, USA*
[4]*National Center for Computational Sciences, Oak Ridge National Laboratory, Oak Ridge, Tennessee 37831, USA*

(Received 18 June 2015; revised manuscript received 6 November 2015; published 24 February 2016)

Chiral effective field theory (χEFT) provides a systematic approach to describe low-energy nuclear forces. Moreover, χEFT is able to provide well-founded estimates of statistical and systematic uncertainties —although this unique advantage has not yet been fully exploited. We fill this gap by performing an optimization and statistical analysis of all the low-energy constants (LECs) up to next-to-next-to-leading order. Our optimization protocol corresponds to a simultaneous fit to scattering and bound-state observables in the pion-nucleon, nucleon-nucleon, and few-nucleon sectors, thereby utilizing the full model capabilities of χEFT. Finally, we study the effect on other observables by demonstrating forward-error-propagation methods that can easily be adopted by future works. We employ mathematical optimization and implement automatic differentiation to attain efficient and machine-precise first- and second-order derivatives of the objective function with respect to the LECs. This is also vital for the regression analysis. We use power-counting arguments to estimate the systematic uncertainty that is inherent to χEFT, and we construct chiral interactions at different orders with quantified uncertainties. Statistical error propagation is compared with Monte Carlo sampling, showing that statistical errors are, in general, small compared to systematic ones. In conclusion, we find that a simultaneous fit to different sets of data is critical to (i) identify the optimal set of LECs, (ii) capture all relevant correlations, (iii) reduce the statistical uncertainty, and (iv) attain order-by-order convergence in χEFT. Furthermore, certain systematic uncertainties in the few-nucleon sector are shown to get substantially magnified in the many-body sector, in particular when varying the cutoff in the chiral potentials. The methodology and results presented in this paper open a new frontier for uncertainty quantification in *ab initio* nuclear theory.

DOI: 10.1103/PhysRevX.6.011019

Subject Areas: Computational Physics, Nuclear Physics, Particles and Fields

I. INTRODUCTION

Uncertainty quantification is essential for generating new knowledge in scientific studies. This insight also resonates in theoretical disciplines, and forward error propagation is gaining well-deserved recognition. For instance, theoretical error bars have been estimated in various fields such as neurodynamics [1], global climate models [2], molecular dynamics [3], density functional theory [4], and high-energy physics [5].

In this paper, we present a systematic and practical approach for uncertainty quantification in microscopic nuclear theory. For the first time, we provide a common statistical regression analysis of two key frameworks in theoretical nuclear physics: *ab initio* many-body methods and chiral effective field theory (χEFT). We supply a set of mathematically optimized interaction models with known statistical properties so that our results can be readily applied by others to explore uncertainties in related efforts.

The *ab initio* methods for solving the many-nucleon Schrödinger equation, such as the no-core shell model (NCSM) [6] and the coupled cluster (CC) approach [7], are characterized by the use of controlled approximations. This provides a handle on the error that is associated with the solution method itself. Over the past decade, there has been significant progress in first-principles calculations of bound, resonant, and scattering states in light nuclei [6,8–12] and medium-mass nuclei [7,13–16]. The appearance of independently confirmed and numerically exact solutions to the nuclear many-body problem has brought forward the need for an optimized nuclear interaction model with high accuracy, quantified uncertainties, and predictive capabilities.

*borisc@chalmers.se
†ekstrom@utk.edu
‡christian.forssen@chalmers.se

χEFT is a powerful and viable approach for describing the low-energy interactions between constituent nucleons [17,18]—a cornerstone for the microscopically grounded description of the atomic nucleus and its properties. Most importantly, the inherent uncertainty of the χEFT model can be estimated from the remainder term of the underlying momentum expansion of the effective Lagrangian. We refer to this error as a systematic model uncertainty.

We use the common term low-energy constants (LECs) to denote the effective parameters of a nuclear interaction model. Indeed, for the description of atomic nuclei, the numerical values of the LECs play a decisive role. In the χEFT approach, the LECs can, in principle, be connected to predictions from the underlying theory of quantum chromodynamics (QCD) (see, e.g., Ref. [19]). However, the currently viable approach to accurately describe atomic nuclei in χEFT requires that the LECs are constrained from experimental low-energy data. The bulk of this fit data traditionally consists of cross sections measured in nucleon-nucleon (NN) scattering experiments. Most often, these data are parametrized in terms of phase shifts [20,21]. However, experimental data come with error bars, which implies that a thorough statistical error analysis of the constructed nuclear Hamiltonian can only be performed when fitting directly to nuclear scattering observables. This optimization procedure gives rise to statistical uncertainties on the LECs.

In general, the determination of the LECs constitutes an extensive nonlinear optimization problem. In other words, the relatively large number of parameters makes it challenging to find optimal values such that the experimental fit data are best reproduced. Various methods and objective functions have been used to solve this problem for a wide array of available nuclear-interaction models [22–28]. More often than not, the parameters of the models were fitted by hand. Mathematical optimization algorithms were only recently introduced in this venture by Ekström *et al.* [29] and by Navarro Perez *et al.* [30]. First attempts to investigate the statistical constraints on the LECs of mathematically optimized interactions have recently been performed in the NN sector with coarse-grained δ-shell interactions [31–34] and with χEFT NN interactions [35,36].

The so-called power-counting scheme of the χEFT approach offers a systematically improvable description of NN, three-nucleon (NNN), and pion-nucleon (πN) interactions. It provides a consistent framework in which LECs from the effective πN Lagrangian also govern the strength of pion exchanges in the NN potential and of long- and intermediate-range NNN forces. This implies that πN scattering data can be used to constrain some LECs that enter the chiral nuclear Hamiltonian.

Furthermore, χEFT offers an explanation for the appearance of many-nucleon interactions, such as NNN diagrams, and the fact that they provide higher-order corrections in the hierarchy of nuclear forces. Still, effective NNN forces are known to play a prominent role in nuclear physics [8,37,38]. Most often, the LECs that are associated with the NNN terms have been determined relative to existing NN Hamiltonians. These LECs are optimized against a few select binding energies, excitation energies, or other properties of light nuclei.

The extended approach that is presented here is conceptually consistent with χEFT in the sense that the $NN + NNN$ Hamiltonian is constrained from a simultaneous mathematical optimization to NN and πN scattering data, plus observables from NNN bound states including the electroweak process responsible for the β decay of ^{3}H. Furthermore, we include the truncation error of the chiral expansion to take systematic theoretical errors into account. If correctly implemented, the truncation error of an observable calculated in this scheme should decrease systematically with increasing order in the χEFT expansion. Indeed, we show that the resulting propagated uncertainties of a simultaneous fit are smaller and exhibit a more obvious convergence pattern compared to the traditional separate or sequential approaches that have been published so far.

Below, we summarize the work presented in this paper by listing three specific objectives:

(i) Establish a systematic framework for performing mathematical optimization and uncertainty quantification of nuclear forces in the scheme of χEFT. Our approach relies on the simultaneous optimization of the effective nuclear Hamiltonian to low-energy πN, NN, and NNN data with the inclusion of experimental as well as theoretical error bars.

(ii) Demonstrate methods to propagate the statistical errors in the order-by-order optimized nuclear Hamiltonian to various nuclear observables and investigate the convergence of the chiral expansion.

(iii) Deliver optimized chiral interactions with well-defined uncertainties and thoroughly introduce the accompanying methodological development such that our results can be easily applied in other calculations.

Our paper is organized as follows: In Sec. II, we introduce the methodology. We start with the construction of the nuclear potential from χEFT and proceed to the calculation of observables and the optimization of parameters. In particular, we introduce automatic differentiation for numerically exact computation of derivatives, and we discuss the error budget and error propagation. The results of our analysis, for potentials at different orders in the chiral expansion and using different optimization strategies, is presented in Sec. III. We study the order-by-order convergence and the correlation between parameters, and we present first results for few-nucleon observables with well-quantified statistical errors propagated via chiral interactions. The consequences of our findings in the few- and many-body sectors are discussed in Sec. IV, and in Sec. V, we present an outlook for further work.

II. METHOD

In this section, we give an overview of the nuclear χEFT that we employ to construct a nuclear potential (Sec. II A). The optimal values for LECs are not provided by χEFT itself; they need to be constrained from a fit to data. For completeness, we summarize the well-known methods to calculate the relevant experimental observables: NN scattering cross sections (Sec. II B), NN $^1S_0$ effective-range parameters (Sec. II C), and bound-state properties for $A \leq 4$ nuclei using the Jacobi-coordinate no-core shell model (Sec. II D). We also present the objective function (Sec. II E), the optimization algorithm (Sec. II F), and the formalism for the statistical regression (Sec. II G).

A. Nuclear potential from χEFT

The long-range part of the nuclear interaction in χEFT is governed by the spontaneously broken chiral symmetry of QCD and mediated by the corresponding Goldstone boson, the pion (π). This groundbreaking insight [39] enables a perturbative approach to the description of phenomena in low-energy nuclear physics [40]. High-energy physics that is not explicitly important is accounted for through a process of renormalization and regularization with an accompanying power-counting scheme. The expansion parameter is defined as Q/Λ_χ, where Q is associated with the external momenta (soft scale) and $\Lambda_\chi \approx M_\rho$ (hard scale), with $M_\rho \approx 800$ MeV the mass of the rho meson. The benefit of a small-parameter expansion is that higher orders contribute less than lower orders. If the series is converging, an estimate of the magnitude of the truncation error is given by the size of the remainder.

The chiral order of a Feynman diagram is governed by the adopted power-counting scheme. Given this, any chiral order $\nu \geq 0$ in the expansion will be identified with a finite set of terms proportional to $(Q/\Lambda_\chi)^\nu$. In this work, we have adopted the standard Weinberg power counting (WPC), which is obtained from the assumptions of naive dimensional analysis. For the scattering of two or more nucleons without spectator particles, ν is determined by (see, e.g., Ref. [18])

$$\nu = 2A - 4 + 2L + \sum_i \Delta_i, \tag{1}$$

where A is the number of nucleons and L is the number of pion loops involved. The sum runs over all vertices i of the considered diagrams, and Δ_i is proportional to the number of nucleon fields and pion-mass derivatives of vertex i. Here, $\Delta_i \geq 0$ for all diagrams allowed by chiral symmetry. In Fig. 1, we show the different interaction diagrams that enter at various orders. For the NN system, contributions at $\nu = 1$ vanish because of parity and time-reversal invariance. Also, we consider nucleons and pions as the only effective degrees of freedom and ignore possible nucleon excitations; i.e., we use the so-called delta-less version of χEFT.

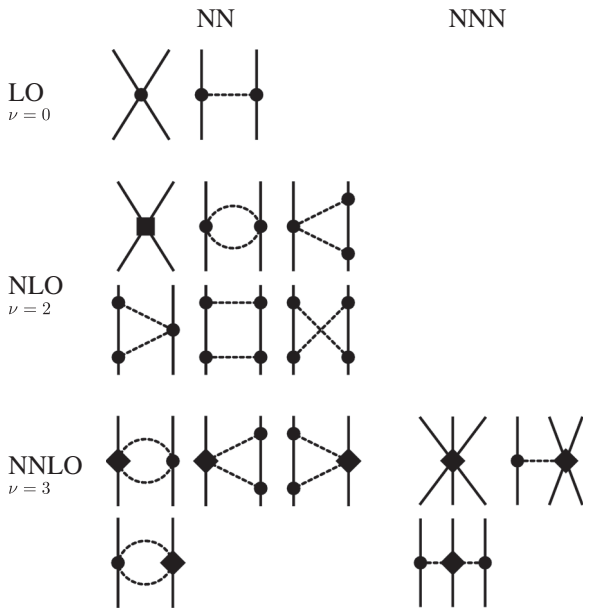

FIG. 1. Schematic overview of the Feynman diagrams present at leading order (LO), next-to-leading order (NLO), and next-to-next-to-leading order (NNLO). Nucleons (pions) are represented by solid (dashed) lines. The NNN interaction enters at NNLO. A circle, diamond, and square represent a vertex of order $\Delta = 0$, 1, and 2, respectively.

The interaction due to short-range physics is parametrized by contact terms, which also serve to renormalize the infinities of the pion loop integrals. The order-by-order expansion of this zero-range contribution is also organized in terms of increasing powers of Q/Λ_χ. Because of parity, only even powers of ν are nonzero. Furthermore, the contact terms of order $\nu = 0$ contribute only to partial waves with angular momentum $L = 0$, i.e., S waves, whereas $\nu = 2$ contact terms contribute up to P waves. In general, the contact interaction at order ν acts in partial waves with $L \leq \nu/2$. Following Eq. (1), the terms in the χEFT expansion, up to third order, are given by a sum of contact interactions $V_{\rm ct}$ and one- plus two-pion exchanges, denoted by $V_{1\pi}$ and $V_{2\pi}$, respectively:

$$\begin{aligned} V_{\rm LO} &= V_{\rm ct}^{(0)} + V_{1\pi}^{(0)}, \\ V_{\rm NLO} &= V_{\rm LO} + V_{\rm ct}^{(2)} + V_{1\pi}^{(2)} + V_{2\pi}^{(2)}, \\ V_{\rm NNLO} &= V_{\rm NLO} + V_{1\pi}^{(3)} + V_{2\pi}^{(3)} + V_{NNN}. \end{aligned} \tag{2}$$

The superscript indicates the separate chiral orders $\nu = 0$, 2, 3, referred to as LO, NLO, and NNLO. For detailed expressions, see, e.g., Ref. [27]. The three-nucleon interaction V_{NNN} contains three different diagrams, as shown in Fig. 1. These correspond to two-pion exchange, one-pion exchange plus contact, and a pure NNN contact term.

Insofar, the analytical expressions for the NN potential have been derived up to fifth order (N4LO) [41,42]. The partial-wave decomposition for the NNN interaction at NNLO is well known [43], while the N3LO contribution was published very recently [44]. Note that the connected four-nucleon diagrams also appear at this higher order. In the present work, we limit ourselves to NNLO for completeness.

The strengths of the terms in the χEFT interaction are governed by a set of LECs. These parameters play a central role in this work, and we discuss in detail how they are constrained from measured data. In general, for each chiral order, there will appear a new set of LECs. For the nuclear interactions used in this work [see Eq. (2)], the corresponding LECs are denoted

$$\begin{aligned} V_{\mathrm{ct}}^{(0)} &\sim \{\tilde{C}_{^1S_0}, \tilde{C}_{^3S_1}\}, \\ V_{\mathrm{ct}}^{(2)} &\sim \{C_{^1S_0}, C_{^3S_1}, C_{E_1}, C_{^3P_0}, C_{^1P_1}, C_{^3P_1}, C_{^3P_2}\}, \\ V_{2\pi}^{(3)} &\sim \{c_1, c_3, c_4\}, \\ V_{NNN} &\sim \{c_1, c_3, c_4, c_D, c_E\}. \end{aligned} \tag{3}$$

Furthermore, there are additional constants that must be determined before making quantitative predictions in χEFT. Here, we set the axial-vector coupling constant to the experimentally determined value of $g_A = 1.276$ [45] for LO, whereas for the higher orders, we use the renormalized value of $g_A = 1.29$ to account for the Goldberger-Treiman discrepancy [27]. At all orders, we use $F_\pi = 92.4$ MeV [27]. All other physical constants, such as nucleon masses and the electric charge, are taken from CODATA 2010 [46], except the pion masses for which we have used the values from the Particle Data Group [47].

Note that LECs that determine the subleading πN interaction vertices occur in both the NN interaction and the two-pion-exchange part of the NNN (see Refs. [27,43]). Besides offering this pion-vertex link between the NN and the NNN interaction, the πN interaction model of χEFT allows us to describe πN scattering processes. Consequently, experimental πN scattering data can be used to constrain the long-range part of the nuclear interaction. The lowest-order terms of the effective πN Lagrangian have $\nu = 1$ and are free from LECs, besides g_A and F_π. At order $\nu = 2$, the LECs c_1, c_2, c_3, and c_4 enter. Higher-order πN LECs, such as $d_1 + d_2$, d_3, d_5, and $d_{14} - d_{15}$, enter at $\nu = 3$, while e_{14} to e_{18} appear at $\nu = 4$. In total, there are 13 LECs in the πN Lagrangian up to fourth order.

The different masses and charges of the up and down quarks give rise to isospin-violating effects [18,27]. There are both short- and long-range isospin-violating effects. The long-range effects are of electromagnetic (EM) origin, and for this contribution, we use the well-known set of potentials

$$\begin{aligned} V_{\mathrm{EM}}^{(pp)} &= V_{\mathrm{C1}} + V_{\mathrm{C2}} + V_{\mathrm{VP}} + V_{\mathrm{MM}}^{(pp)}, \\ V_{\mathrm{EM}}^{(np)} &= V_{\mathrm{MM}}^{(np)}, \end{aligned} \tag{4}$$

where C1 is the static Coulomb potential, C2 the relativistic correction to the Coulomb potential [48], VP the vacuum polarization potential [49], and MM the magnetic-moment interaction [50]. The long-range effects become increasingly important as the scattering energy approaches zero; consequently, we include all the above long-range effects at all orders in the chiral expansion. We also consider short-range isospin-breaking mechanisms. At NLO, the $\tilde{C}_{^1S_0}$ contact is split into three charge-dependent terms: $\tilde{C}_{^1S_0}^{(pp)}$, $\tilde{C}_{^1S_0}^{(np)}$, and $\tilde{C}_{^1S_0}^{(nn)}$. At this order, and above, we also take the pion-mass splitting into account in one-pion exchange terms [18].

An effective field theory often has to handle more than one expansion parameter. In our case, the nucleon mass, $M_N \equiv 2M_pM_n/(M_p + M_n)$, where M_p (M_n) is the proton (neutron) mass, provides such an extra scale, and the use of the heavy-baryon chiral perturbation theory introduces relativistic corrections with factors of $1/M_N$. We count these corrections as $Q/M_N \approx (Q/\Lambda_\chi)^2$ [40,51]. This choice implies that no relativistic corrections appear in the NN sector up to the order considered in this paper.

To regularize the loop integrals that are present in the two-pion exchange diagrams, we employ spectral function regularization (SFR) [52] with an energy cutoff $\tilde{\Lambda} = 700$ MeV. The nuclear interaction is calculated perturbatively in χEFT. A nuclear potential that can be used for bound and scattering states is obtained by iterating the terms of the chiral expansion in the Lippmann-Schwinger or Schrödinger equation [53]. We employ the minimal-relativity prescription from Ref. [54] to obtain relativistically invariant potential amplitudes. The ultraviolet-divergent Lippmann-Schwinger equation also requires regularization. We remove high-momentum contributions beyond a cutoff energy Λ by multiplying the NN and NNN interaction terms with standard (nonlocal) regulator functions $f_{NN}(p)$ and $f_{NNN}(p,q)$, respectively,

$$f_{NN}(p) = \exp\left[-\left(\frac{p}{\Lambda}\right)^{2n}\right] \tag{5}$$

and

$$f_{NNN}(p,q) = \exp\left[-\left(\frac{4p^2 + 3q^2}{4\Lambda^2}\right)^{n}\right], \tag{6}$$

where p and q are the Jacobi momenta of the interacting nucleons. In this work, we mainly use $\Lambda = 500$ MeV and $n = 3$. However, we also explore the consequences of varying Λ in steps of 25 MeV between 450 and 600 MeV. The canonical power-counting, i.e., WPC, and

the nonperturbative renormalization of nuclear χEFT in its current inception are currently under some debate [55,56]. In relation to this, it should be stressed that our implementation of statistical regression methods and gradient-based optimization methods furnishes an independent framework to extract well-founded estimates of the uncertainties in theoretical few-nucleon physics and a tool to assess the convergence properties of χEFT.

B. Nuclear scattering

The NN scattering observables are calculated from the spin-scattering matrix M [57,58]. This is a 4×4 matrix in spin space that operates on the initial state to give the scattered part of the final state. Thus, M is related to the conventional scattering matrix S by $M=(2\pi/ip)(S-1)$, where p is the relative momentum between the nucleons. The decomposition of M into partial waves is given by (see, e.g., Ref. [20])

$$M^{s's}_{m'm}(\theta,\phi)=\frac{\sqrt{4\pi}}{2ip}\sum_{J,L,L'}(-1)^{s-s'}i^{L-L'}\hat{J}^2\hat{L}Y^{L'}_{m-m'}(\theta,\phi)\times\begin{pmatrix}L' & s' & J\\ m-m' & m' & -m\end{pmatrix}\begin{pmatrix}L & s & J\\ 0 & m & -m\end{pmatrix}\times\langle L',s'|S^J-1|L,s\rangle, \tag{7}$$

where the big parentheses are Wigner $3j$ symbols, s (s') and m (m') are initial (final) total spin and spin projection, respectively, $\mathbf{J}=\mathbf{L}+\mathbf{s}$ is the total relative angular momentum, and $\hat{L}$ ($\hat{J}$) is $2L+1$ ($2J+1$). The quantization axis is taken along the direction of the incoming nucleon, and θ gives the center-of-mass scattering angle. The S matrix for the scattering channel with angular momentum J can be parametrized by the Stapp phase shifts [59],

$$S^J_{L=J\pm1}=\begin{pmatrix}e^{2i\delta_{J-1,J}}\cos 2\epsilon_J & ie^{i(\delta_{J-1,J}+\delta_{J+1,J})}\sin 2\epsilon_J\\ ie^{i(\delta_{J-1,J}+\delta_{J+1,J})}\sin 2\epsilon_J & e^{2i\delta_{J+1,J}}\cos 2\epsilon_J\end{pmatrix} \tag{8}$$

for the coupled triplet channel, and

$$S^J_{L=J}=\begin{pmatrix}e^{2i\delta_J}\cos 2\gamma_J & ie^{i(\delta_J+\delta_{J,J})}\sin 2\gamma_J\\ ie^{i(\delta_J+\delta_{J,J})}\sin 2\gamma_J & e^{2i\delta_{J,J}}\cos 2\gamma_J\end{pmatrix} \tag{9}$$

for the (coupled) singlet-triplet channel with $L=J$.

The spin-singlet ($S=0$) phase shift is denoted by $\delta_{L=J}$ and the spin-triplet ($S=1$) phase shift by $\delta_{L,J}$, while ϵ_J represents the triplet-channel mixing angle and γ_J is the spin-flip mixing angle [60] ($\gamma_J=0$ for pp scattering).

In practice, the infinite sums in Eq. (7) are truncated at L, $L'\le L_{\max}$. Calculations that involve long-ranged EM effects require $L_{\max}\ge 1000$ in order to reach convergence, while $L_{\max}=30$ is sufficient for the part coming from the short-ranged nuclear interaction. This leads to a natural separation of the terms in Eq. (7); see, e.g., Ref. [50]. In brief, all EM amplitudes are calculated independently in Coulomb Distorted-Wave Born Approximation (CDWBA) using Vincent-Phatak matching [61] to handle the difficulties of the Coulomb interaction in momentum space. For the $^1S_0$ channel, the C2 and VP interactions are strong enough that a small correction to the bare phase shifts is needed, resulting in

$$\delta_{\text{total}}=\delta^{(\text{CDWBA})}_{\text{C1}+NN}+\tilde{\Delta}_0-\rho_0-\tau_0, \tag{10}$$

where $\delta^{(\text{CDWBA})}_{\text{C1}+NN}$ is the phase shift of the Coulomb and the chiral NN interactions computed in CDWBA, ρ_0 (τ_0) is the C2 (VP) phase shift in CDWBA, and $\tilde{\Delta}_0$ is a correction calculated by interpolating between the values tabulated by Bergervoet *et al.* [62]. In principle, $\tilde{\Delta}_0$ is dependent on the interaction model for the strong force; this effect has been shown to be very small [62] and was not considered here.

We compute the VP phase shifts τ_L in CDWBA using the variable-phase method [63]. The values we obtain agree with the ones that are tabulated by Bergervoet *et al.* [62]. The VP amplitude is calculated in the first-order approximation derived by Durand [49] using the expansion parameter $X\equiv 4m_e^2/[T_{\text{lab}}M_p(1-\cos(\theta))]$, where m_e is the electron mass. We find that $X\lesssim 0.031$ for all scattering data that are employed in this work. The MM amplitude for np and pp scattering is given by Stoks[1] [50].

The Stapp phase shifts are calculated from the real-valued free reaction matrix R [64], which is defined through a Lippman-Schwinger-type equation [64]

$$R^{S,J}_{L'L}(p',p)=V^{S,J}_{L'L}(p',p)-2\mu\times\sum_{L''}\mathcal{P}\int_0^\infty p''^2\mathrm{d}p''\frac{V^{S,J}_{L'L''}(p',p'')R^{S,J}_{L''L}(p'',p)}{p''^2-p^2}, \tag{11}$$

where V is the potential, μ is the reduced mass, and $\mathcal{P}$ denotes the Cauchy principal value.

Because of parity and time-reversal invariance, the scattering matrix M has six linearly independent elements. We employ the Saclay parametrization [57], with complex amplitudes a to f, to express

[1]Note that Eq. (24) in Ref. [50] has the wrong sign. Furthermore, Eq. (25) should have $|\sin(\theta)|$.

$$M(\mathbf{q},\mathbf{k}) = \frac{1}{2}\{(a+b)+(a-b)\boldsymbol{\sigma}_1\cdot\hat{\mathbf{r}}\boldsymbol{\sigma}_2\cdot\hat{\mathbf{r}} + (c+d)(\boldsymbol{\sigma}_1\cdot\hat{\mathbf{q}})(\boldsymbol{\sigma}_2\cdot\hat{\mathbf{q}}) + (c-d)(\boldsymbol{\sigma}_1\cdot\hat{\mathbf{k}})(\boldsymbol{\sigma}_2\cdot\hat{\mathbf{k}}) - e(\boldsymbol{\sigma}_1+\boldsymbol{\sigma}_2)\cdot\hat{\mathbf{r}} - f(\boldsymbol{\sigma}_1-\boldsymbol{\sigma}_2)\cdot\hat{\mathbf{r}}\}, \quad (12)$$

where $\mathbf{q}=\mathbf{p}'-\mathbf{p}$ is the momentum transfer, $\mathbf{k}=(\mathbf{p}'+\mathbf{p})/2$, and $\mathbf{r}=\mathbf{q}\times\mathbf{k}$. For identical particles, f will be zero. Expressions for the scattering observables in terms of the Saclay parameters can be found in Ref. [57] for identical particles and in Ref. [58] for the more general case of nonidentical particles.

For the theoretical description of the πN scattering observables, we use the fourth-order χEFT expressions according to Refs. [65,66]. A detailed description of the EM amplitudes that we employ is given in Refs. [67–70].

C. Effective-range parameters

The effective-range expansion (ERE) of low-energy phase shifts [71] provides parameters that can be directly compared to experimentally inferred values. The ERE can be expressed in the general form

$$A(p)+B(p)p\cot(\delta^{\mathrm{LR}}_{\mathrm{LR}+NN}) = -\frac{1}{a}+\frac{1}{2}r^2p^2+O(p^4). \quad (13)$$

The functions $A(p)$ and $B(p)$ depend on the choice of included long-range EM effects, and $\delta^{\mathrm{LR}}_{\mathrm{LR}+NN}$ is the phase shift of the total nuclear potential (long-range plus strong NN) relative to the phase shift of only the long-range part.

For nn and np scattering, we have $A(p)=0$ and $B(p)=1$ [71] since there are no EM effects. The corresponding ERE parameters are denoted a^{N}_{nn}, r^{N}_{nn}, a^{N}_{np}, and r^{N}_{np}.

For pp scattering, we calculate ERE parameters for the nuclear plus Coulomb potential, i.e., using the phase shifts $\delta^{(\mathrm{CDWBA})}_{\mathrm{C1}+NN}$. The expressions for $A_C(p)$ and $B_C(p)$ can be found in Refs. [62,71]. The corresponding ERE parameters are denoted a^C_{pp} and r^C_{pp}.

In practice, the ERE parameters are determined using a linear least-squares fit to 20 equally spaced phase shifts in the $T_{\mathrm{lab}}=10$–100 keV range.

D. Few-nucleon observables

We employ the Jacobi-coordinate version of the NCSM [72] to compute bound-state observables for ^{2,3}He and ^{3,4}He. Apart from binding energies and radii, we also compute the deuteron quadrupole moment $Q(^2\mathrm{H})$ and the comparative half-life for the triton, $fT_{1/2}(^3\mathrm{H})$.

In the NCSM, observables and wave functions are obtained from the exact solution of the eigenvalue problem $\mathcal{H}|\psi\rangle = E|\psi\rangle$. In this work, the nuclear Hamiltonian $\mathcal{H}$ is given by

$$\mathcal{H} = \sum_{i<j=1}^{A} T_{ij} + \sum_{i<j=1}^{A} V_{ij} + \sum_{i<j<k=1}^{A} V_{ijk}, \quad (14)$$

where T_{ij} are relative kinetic energies while V_{ij} and V_{ijk} are the NN and NNN interactions, respectively. In our calculations, we use the isoscalar approximation as presented in Ref. [73]. The model-space dimension is determined from the maximal number of allowed harmonic-oscillator (HO) excitations $N_{\max}$. We obtain essentially converged results in a HO basis with oscillator energy $\hbar\omega = 36$ MeV and model-space dimension $N_{\max}=40(20)$ for $A=3(4)$.

The experimentally measured electric-charge radius can be related to the theoretically calculated point-proton radius through the relation [74]

$$r^2_{\text{pt-p}} = r^2_{\mathrm{ch}} - r^2_p - \frac{N}{Z}r^2_n - r^2_{\mathrm{DF}} - \Delta r^2, \quad (15)$$

where r^2_p (r^2_n) is the proton (neutron) charge mean-squared radius and Z (N) is the proton (neutron) number. Furthermore, $r^2_{\mathrm{DF}} \equiv (3/4M^2_N)$ is the Darwin-Foldy correction [75], and Δr^2 includes effects of two-body currents and further relativistic corrections. We use $r_p = 0.8783(86)$ fm and $r^2_n = -0.1149(27)$ fm^2 [76]. For all nuclei, we use $\Delta r^2 = 0$.

Precise results for electroweak observables depend on two-body nuclear currents and relativistic effects. χEFT provides a consistent framework for including such corrections and for deriving quantum-mechanical currents, such as the electroweak one, from the same Lagrangian as the nuclear force. We follow the approach by Gazit *et al.* [77] and compute the triton half-life from the reduced matrix element for E^A_1, the $J=1$ electric multipole of the axial-vector current

$$\langle E^A_1\rangle \equiv |\langle {}^3\mathrm{He}\|E^A_1\|{}^3\mathrm{H}\rangle|. \quad (16)$$

This matrix element is proportional to c_D, the LEC that also determines the strength of the $NN-\pi N$ diagram of the NNN interaction. As a consequence, the triton half-life provides a further constraint of the nuclear force. The experimentally determined comparative half-life, $fT_{1/2} = 1129.6 \pm 3$ s [78], leads to an empirical value for $\langle E^A_1\rangle = 0.6848 \pm 0.0011$ [77].

We choose to use the value $Q_{\mathrm{d}} = 0.27$ e fm^2 for the deuteron quadrupole moment, obtained from a theoretical calculation [24] using the high-precision, meson-exchange NN model CD-Bonn. In order to cover the spread in values obtained using other NN potential models [18], we introduce a conservative error estimate of 4% for this observable.

E. Objective function

Using the methods to compute observables outlined above, the vector $\boldsymbol{\alpha}$ of numerical values for the LECs at a given order in χEFT is constrained using experimental data. This is accomplished by minimizing an objective function defined as

$$\chi^2(\boldsymbol{\alpha}) \equiv \sum_{i\in\mathbb{M}} \left(\frac{\mathcal{O}_i^{\rm theo}(\boldsymbol{\alpha}) - \mathcal{O}_i^{\rm exp}}{\sigma_i} \right)^2 \equiv \sum_{i\in\mathbb{M}} r_i^2(\boldsymbol{\alpha}), \qquad (17)$$

where $\mathcal{O}_i^{\rm theo}$ and $\mathcal{O}_i^{\rm exp}$ denote the theoretical and experimental values of observable $\mathcal{O}_i$ in the pool of fit data $\mathbb{M}$, and the total uncertainty σ_i determines the weight of the residual, r_i. The optimal set of LECs $\boldsymbol{\alpha}_\star$ is defined from

$$\boldsymbol{\alpha}_\star = \underset{\boldsymbol{\alpha}}{\rm argmin}\chi^2(\boldsymbol{\alpha}). \qquad (18)$$

We wish to explore the physics capabilities and limitations of nuclear χEFT by forming different objective functions and subsequently probing the precision and accuracy of each one in a statistical regression analysis [79]. At each chiral order (LO, NLO, or NNLO), we compare two different strategies of minimization: simultaneous (sim) and separate (sep). In the "separate" approach, we first optimize the subleading πN LECs (c_i, d_i, e_i) using πN data. Subsequently, we optimize the NN contact potential of the nuclear interaction using NN scattering data, and finally (at NNLO), the NNN interaction is determined by fitting c_D and c_E to the known binding energies and radii of ^{3}H and ^{3}He, and the comparative β-decay half-life of ^{3}H. Besides the first-ever application of novel derivative-based optimization techniques to this problem, the separate approach is very similar to the conventional procedure to constrain the description of the nuclear interaction. In contrast, with the "simultaneous" approach, we optimize all the LECs up to a specific order in χEFT at the same time with respect to NN and πN scattering data as well as experimentally determined bound-state observables in the two- and three-nucleon systems: ^{2,3}H and ^{3}He. At LO and NLO, the NN interaction does not involve any subleading πN amplitudes, nor are there any NNN force terms. Therefore, at these orders, the sim potentials are optimized using only NN scattering data and the binding energy, radius, and quadrupole moment of the deuteron. A summary of the data types that were included in the objective function for each potential is given in Table I.

The bulk of the experimental data consist of NN and πN scattering cross sections. For the NN data, we take the SM99 database [21] entries with laboratory scattering energies $T_{\rm Lab} \leq T_{\rm Lab}^{\rm max} = 290$ MeV, i.e., the pion-production threshold, which constitutes a natural limit of applicability for χEFT. This results in $N_{\rm data}^{(pp)} = 2045$ and $N_{\rm data}^{(np)} = 2400$ data points, including normalization data. The number of normalization constants are $N_{\rm norm}^{(pp)} = 124$ and $N_{\rm norm}^{(np)} = 148$. However, we also explore the consequences of varying $T_{\rm Lab}^{\rm max}$ between 125 and 290 MeV. Unless otherwise stated, our canonical choice is $T_{\rm Lab}^{\rm max} = 290$ MeV and $\Lambda = 500$ MeV. As there are no neutron-neutron scattering data, we use the neutron-neutron $^1S_0$ scattering length $a_{nn}^{\rm N} = -18.95(40)$ fm [18] and effective range $r_{nn}^{\rm N} = 2.75(11)$ fm [80] to constrain the parameter $\tilde{C}_{^1S_0}^{(nn)}$ at order NLO. For the πN scattering observables, we employ the database from the Washington Institute group [81], here referred to as the WI08 database. The πN data consist mainly of differential cross sections and some singly-polarized differential cross sections for the processes $\pi^\pm + p \to \pi^\pm + p$ and $\pi^- + p \to \pi^0 + n$. Unfortunately, the WI08 database contains very little data at low scattering energies, which would have been preferred to constrain the low-energy theory of χEFT. In fact, there is no scattering data below $T_{\rm lab} = 10.6$ MeV. For this reason, we include all data up to lab energy $T_{\rm lab} = 70$ MeV and keep all terms up to, and including, $\nu = 4$ when calculating πN observables. A lower chiral order does not give a reasonable description of the data. This results in $N_{\rm data}^{(\pi{\rm N})} = 1347$ data points including $N_{\rm norm}^{(\pi{\rm N})} = 110$ normalization data. At the optimum, it is usually assumed that the residuals are normally distributed and that they are all independent of each other. If so, then $\chi^2(\boldsymbol{\alpha}_\star)$ will comply with a chi-squared distribution with $N_{\mathbb{M}} - N_{\rm norm} - N_\alpha \equiv N_{\rm edf} - N_\alpha \equiv N_{\rm dof}$ degrees of freedom, where N_α denotes the number of LECs (i.e., the number of model parameters). In turn, this allows for a standard regression analysis. These rather strong assumptions of both the model and the data are only approximately fulfilled, mainly because of the inherent systematic error in χEFT.

TABLE I. Objective functions for the various nuclear interactions in this work. Included data types are marked with "X." For sequential optimization, the subscript "i" indicates at what stage the model is optimized to that data. Excluded data types are indicated with "…".

	Scattering data		nn ERE	Bound-state data	
Potential	NN	πN	$a_{nn}^{\rm N}$, $r_{nn}^{\rm N}$	^{2}H	^{3}H, ^{3}He
LOsep	X	…	…	…	…
LOsim	X	…	…	X	…
NLOsep	X_1	…	X_2	…	…
NLOsim	X	…	X	X	…
NNLOsep	X_2	X_1	…	…	X_3
NNLOsim	X	X	…	X	X

The distribution of residuals, r_i, for the NNLOsim potential, which will be thoroughly introduced in Sec. III A, is shown in Fig. 2. It is clear that the residuals are not entirely normally distributed, with a skewness of $-0.38(3)$ and excess kurtosis of 5.39(6). The main reason

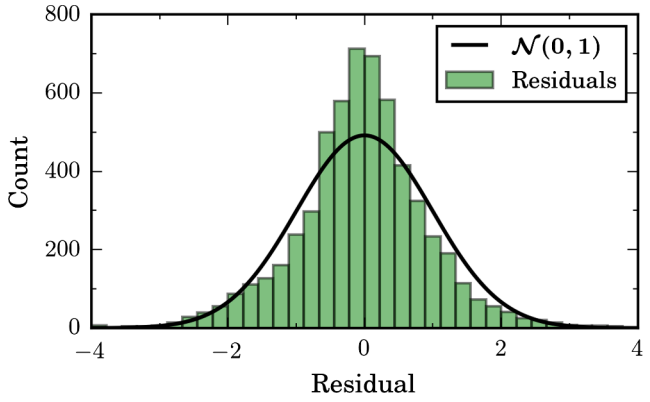

FIG. 2. Residual distribution for the NNLOsim potential, with a sample mean and standard deviation of $-0.04(1)$ and 0.977(9), respectively. The deviations from normality, as discussed in the text, are mainly due to the model error of χEFT.

for this deviation can be traced to the inclusion of a systematic error in the fit. This can produce a consistent overestimate or underestimate of observables, resulting in a nonzero skewness. A nonzero excess kurtosis indicates that the model error sometimes overestimates the uncertainty and, in other cases, underestimates it, causing a too-sharp peak near zero in the histogram in Fig. 2. We stress that the deviations from normality do not invalidate the use of $\chi^2(\boldsymbol{\alpha})$ as an objective function to fit the parameters; it just indicates that the minimizer $\boldsymbol{\alpha}_\star$ will not be a maximum-likelihood estimator. In fact, we find that when optimizing NNLOsim using *NN* scattering data up to 125 MeV only, to avoid large model errors, the skewness and excess kurtosis of the *NN* scattering residuals are significantly reduced; $-0.01(6)$ and 0.6(1), respectively. Still, the propagated uncertainties are very similar in these two cases. Thus, the minimization and subsequent regression analysis of the $\chi^2(\boldsymbol{\alpha})$ function will provide valuable insights into both the model and the data [79].

1. Total error budget

For each residual, the total uncertainty σ^2 is divided into an experimental part and a theoretical part,

$$\begin{aligned}\sigma^2 &= \sigma^2_{\text{exp}} + \sigma^2_{\text{theo}} \\ &= \sigma^2_{\text{exp}} + \sigma^2_{\text{numerical}} + \sigma^2_{\text{method}} + \sigma^2_{\text{model}}. \end{aligned} \tag{19}$$

The experimental uncertainty (statistical or systematic) is provided by the experimenter. Here, we focus on estimating the theoretical uncertainty. As a first step, we identify three different components: (1) the numerical error originating in finite computational precision, (2) the method error due to mathematical approximations in the solution of the bound-state or scattering problem, and (3) the model error that is inherent to the truncation of the momentum expansion in χEFT.

The numerical error is the smallest one, and several new technical developments, such as automatic differentiation for computing derivatives, allow us to generally ignore $\sigma^2_{\text{numerical}}$. However, some elements of the statistical analysis can potentially become numerically unstable if the relative errors are too small. In particular, this concerns the computation of the covariance matrix through the inversion of the Hessian (33). For this reason, we impose a minimum relative uncertainty of 0.01%. In practice, this requirement only affects the error of the deuteron binding energy.

Regarding the method error, the only significant contributions come from truncating the NCSM model space and from the use of the isoscalar approximation in calculations of bound-state observables. Indeed, for all scattering cross sections, we include sufficiently many partial waves to construct an exact scattering matrix. We estimate the method error of the NCSM calculations using a simple exponential extrapolation, $\mathcal{O}(N_{\text{max}}) = \mathcal{O}_\infty + a\exp(-bN_{\text{max}})$, for a range of different χEFT potentials. However, for the ground-state energies of three- and four-nucleon systems, the uncertainties from the isoscalar approximation dominate the truncation error by an order of magnitude. We therefore use the uncertainties presented in Ref. [73] as our method error for those energies.

In practice, we combine the method errors with the experimental ones to obtain the resulting weight of each bound-state observable in the optimization (see Table II). In certain cases, the method error is comparative to, or larger than, the experimental error.

TABLE II. Experimentally determined values and uncertainties for ground-state energies (in MeV) and radii (in fm) for ^{2,3}H and ^{3,4}H. The quadrupole moment $Q(^2\text{H})$ of the deuteron is given in e fm^2, and E^A_1 denotes the reduced transition matrix element related to the β decay of ^{3}H. The last column gives the combined experimental and method errors. For the ground-state energies, the method error is much larger than the experimental one. Table I indicates which observables are included in the optimization. Note that the ^{4}He properties are not included in the objective function.

	Experimental value	Reference	$\sigma_{\text{exp+method}}$
$E(^2\text{H})$	$-2.22456627(46)$	[46]	0.22×10^{-3}
$E(^3\text{H})$	$-8.4817987(25)$	[46]	0.028
$E(^3\text{He})$	$-7.7179898(24)$	[46]	0.019
$E(^4\text{He})$	$-28.2956099(11)$	[46]	0.11
$r_{\text{pt-p}}(^2\text{H})$	1.97559(78)[a]	[76,82]	0.79×10^{-3}
$r_{\text{pt-p}}(^3\text{H})$	1.587(41)	[76]	0.041
$r_{\text{pt-p}}(^3\text{He})$	1.7659(54)	[76]	0.013
$r_{\text{pt-p}}(^4\text{He})$	1.4552(62)	[76]	0.0071
$Q(^2\text{H})$	0.27(1)[b]		0.01
$E^1_A(^3\text{H})$	0.6848(11)	[77]	0.0011

[a]The experimental value is $r^2_{\text{ch}}(^2\text{H}) - r^2_p$; we still use the value of r^2_n from Ref. [76].
[b]This is not an empirical value (see the text for details).

The model errors can be labeled as systematic and are the most difficult to assess. We follow the most naive χEFT estimate and associate a truncation error with the effect of excluded higher-order Feynman diagrams. The χEFT expansion up to a given chiral order ν includes all diagrams that scale as $(Q/\Lambda_\chi)^\nu$, where $Q \in \{p, m_\pi\}$. The remainder of the diagrams could *a priori* be assumed to be proportional to $(Q/\Lambda_\chi)^{\nu+1}$.

For bound-state properties, it is not straightforward to associate a relevant and system-dependent momentum scale; therefore, we will not include systematic theoretical errors for these observables. Scattering observables, on the other hand, have a well-defined center-of-mass momentum. As described in Sec. II B, M-matrix elements are the fundamental quantities that are needed to calculate NN scattering observables, and they can be parametrized by the complex-valued Saclay amplitudes a to f. Similarly, the πN non-spin-flip and spin-flip amplitudes $g^\pm$ and $h^\pm$ determine the πN scattering observables [66]. Therefore, from the above scaling argument, we introduce a model error in the scattering amplitudes of the form

$$\sigma^{(\mathrm{amp})}_{\mathrm{model,x}} = C_{\mathrm{x}} \left(\frac{Q}{\Lambda_\chi}\right)^{\nu_{\mathrm{x}}+1}, \qquad \mathrm{x} \in \{NN, \pi N\}, \quad (20)$$

where C_{NN} and $C_{\pi N}$ are two overall constants that need to be determined.

We assume that both the real and the imaginary parts of the Saclay amplitudes $a - e$ scale in this manner. The nuclear force does not contribute to the f amplitude, so we do not impose a model error in that amplitude. Since the order of magnitude of each scattering amplitude is the same, we assign the same constant of proportionality to all of them (see, e.g., Fig. 3). The same argument applies to the πN amplitudes.

We set $Q = p$ to capture the increasing uncertainty in the model as the energy increases. The definition $Q = \max\{p, m_\pi\}$ [17] seems to have a comparatively small impact on the theoretical predictions of the model, as discussed further in Sec. III C.

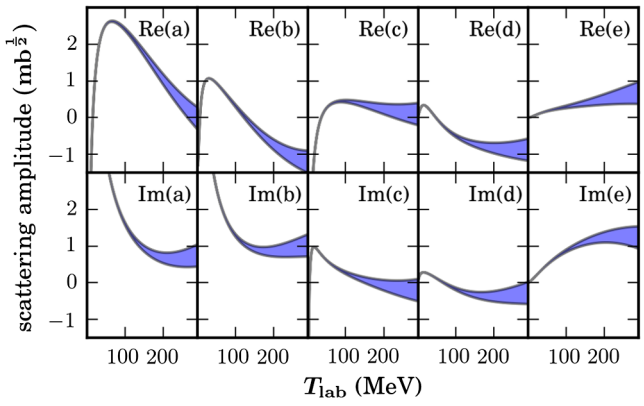

FIG. 3. Saclay amplitudes a to e at a $\theta_{\mathrm{cm}} = 45°$ scattering angle for the potential NNLOsim. The model error bands were extracted according to the discussion in the text.

To determine C_{NN} and $C_{\pi N}$, we use the statistical guiding principle that χ^2/N_{dof} for both NN and πN scattering should be 1 if the objective function χ^2 follows a chi-squared distribution and all errors have been correctly accounted for. This leads to an iterative process where first the C_{x} constants are updated, then the LECs are optimized using the previously determined C_{x}, and so on until the values of the constants have stabilized. This usually requires no more than three iterations.

F. Optimization algorithms

The minimization of $\chi^2(\boldsymbol{\alpha})$, Eq. (17), is a nonlinear optimization problem. In this work, we have employed three different nonlinear least-squares minimization methods at different stages during the optimization: POUNDerS [83], Levenberg-Marquardt (LM), and Newton's method. POUNDerS is part of the TAO package [84] and is a so-called derivative-free method. As the label indicates, it does not require the computation of any derivatives. This makes it very attractive for use with applications where differentiation is a formidable task, e.g., nuclear energy density optimization [85] and previous optimizations of chiral interactions [29,35,86]. However, in this work, we have managed to make significant progress in the optimization problem by implementing automatic differentiation, which enables us to extract machine-precise derivatives of the objective function. Consequently, the whole class of derivative-based optimization algorithms becomes readily available. The convergence rate is increased considerably with the LM method that employs first-order derivatives of the residuals with respect to the LECs. A further improvement can be achieved with Newton's method, which also uses the second-order derivatives. At LO, the presence of only two LECs to parametrize the potential makes it a trivial task to minimize the corresponding objective functions. However, already at the next order, NLO, the optimization requires quite an effort. There are 11 LECs, and in order to provide a reasonable start vector $\boldsymbol{\alpha}_0$ of numerical values for these, we make an initial fit to the NN scattering phase shifts published by the Nijmegen group [20]. At NNLO, there is a total of 26 LECs since we also need to include all 13 πN LECs up to order $\nu = 4$. Also at this order, we carry out an initial fit to NN phase shifts before proceeding with the optimization of the complete objective function. The optimization with respect to scattering observables in the πN sector could proceed without any fits to phase shifts.

There is always a risk of getting trapped in local minima, and the success of the minimization strongly depends on the starting point $\boldsymbol{\alpha}_0$. Extensive searches were performed to search for a global minimum, which is described in more detail in Sec. III A.

1. Automatic differentiation

First- and second-order derivatives of $\chi^2(\boldsymbol{\alpha})$ with respect to the LECs are needed during the minimization process and the subsequent statistical regression analysis; i.e., we need to compute

$$\frac{\partial \mathcal{O}_i^{(\mathrm{theo})}(\boldsymbol{\alpha})}{\partial \alpha_m}, \quad \forall\ i, m,$$
$$\frac{\partial^2 \mathcal{O}_i^{(\mathrm{theo})}(\boldsymbol{\alpha})}{\partial \alpha_m \partial \alpha_n}, \quad \forall\ i, m, n. \tag{21}$$

The straightforward numerical approach is to approximate the nth-order derivatives with finite differences. The general idea is to form appropriate linear combinations of M function evaluations in the vicinity of the point of interest. There are, however, a number of issues with this method. First, it is prone to large numerical errors since differences of large, almost equal, numbers are needed. Second, the result can be very sensitive to the choice of step size. Furthermore, it is also a computationally demanding method since the number of required function evaluations grows quickly with the number of dependent variables and order of the derivative. For instance, a third-order, finite-difference calculation of first and second derivatives with respect to all 26 LECs requires $M = 3653$ function evaluations. For these reasons, we abandon finite-difference methods and employ instead forward-mode automatic differentiation (AD). The basic idea of AD is the following: A computer implementation for calculating the observables, or any computational algorithm for that matter, will consist of a chain of simple (or intrinsic) mathematical operations, e.g., addition and multiplication, elementary functions such as sin and exp, and matrix operations. Therefore, by repeatedly employing the chain rule, derivatives with respect to the LECs can be calculated alongside the usual function evaluations. Using AD, the derivatives of Eq. (21) can actually be computed to machine precision, which is far beyond the precision of any reasonable finite-difference scheme. This accomplishment is illustrated in Fig. 4, where the dependence on the step size for the finite-difference method is also shown for comparison.

We implement forward-mode AD using the Rapsodia computational library [87]. For the calculation of first and second derivatives with respect to N_α different LECs, Rapsodia requires a total of

$$M = 2\binom{N_\alpha + 1}{2} \tag{22}$$

derivative calculations. For $N_\alpha = 26$, this results in $M = 702$, thus considerably more efficient than the finite-difference approach. Furthermore, all calculations that do not depend on the LECs are performed only once, compared to the brute-force implementation of the finite-difference scheme that requires a full calculation for every function evaluation. Furthermore, since all LECs enter linearly in the momentum-space formulation of the chiral potential, it is very easy to calculate the derivatives of the potential with respect to the LECs. Thus, the only workhorses in our calculations are the R-matrix evaluation (matrix inversion) of the scattering process and the solution to the NCSM eigenvalue problem (matrix diagonalization), as we discuss next.

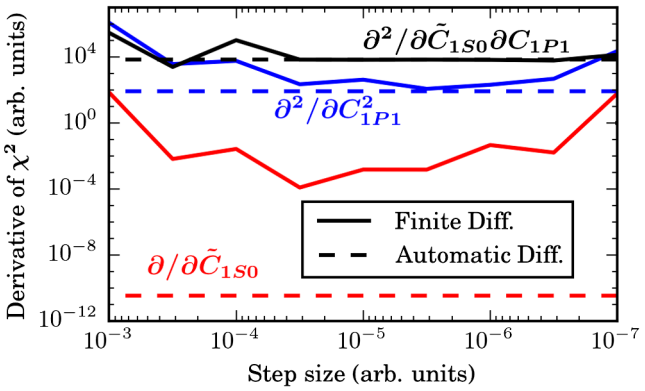

FIG. 4. Comparison between calculated first and second derivatives of an objective function using finite differences (third order) with different step sizes (filled lines) and automatic differentiation (dashed lines). The calculation is done at a minimum where the first derivatives should be approximately zero. Because of cancellation effects, the finite-difference method cannot correctly reproduce the low values of the derivatives for any step size.

To solve for the two-nucleon R matrix (11) at a given on-shell scattering energy, we use the well-known method of Ref. [88]. It recasts the Lippmann-Schwinger equation into a matrix equation

$$(I + VZ)R = V, \tag{23}$$

where I is the identity matrix, V is the two-nucleon potential, and Z is a simple diagonal matrix defined in Ref. [88]. The R matrix is easily obtained after inverting $(I + VZ)$ using, e.g., LU factorization. First- and second-order derivatives of the R matrix with respect to LECs α_x and α_y are easily obtained using the AD technology and the same LU factorization,

$$(I + VZ)\frac{\partial R}{\partial \alpha_x} = \frac{\partial V}{\partial \alpha_x}(I - ZR) \tag{24}$$

$$(I + VZ)\frac{\partial^2 R}{\partial \alpha_x \partial \alpha_y} = \frac{\partial^2 V}{\partial \alpha_x \partial \alpha_y}(I - ZR) - \frac{\partial V}{\partial \alpha_x} Z \frac{\partial R}{\partial \alpha_y} - \frac{\partial V}{\partial \alpha_y} Z \frac{\partial R}{\partial \alpha_x}. \tag{25}$$

We also use the fact that many derivatives are exactly zero, for example, the πN LECs d_i and e_i do not appear in

the formalism for NN scattering at the present chiral orders. The computational overhead of AD in terms of wall time is very small. On a single computational node, the calculation of all first- and second-order derivatives of the 4450 NN scattering observables with respect to the 26 LECs at NNLO only takes twice as long as computing just the central values.

It is straightforward, but slightly more costly, to apply the AD technology to the NCSM diagonalization of the nuclear Hamiltonian $\mathcal{H}$ for $A \leq 4$. If the eigenvalue spectrum is nondegenerate, the first-order derivatives of the ground-state energy E_0 and wave function $|\psi_0\rangle$ with respect to the LEC α_x are given by [89]

$$\frac{\partial E_0}{\partial \alpha_x} = \langle \psi_0 | \frac{\partial \mathcal{H}}{\partial \alpha_x} | \psi_0 \rangle, \tag{26}$$

$$\frac{\partial}{\partial \alpha_x} |\psi_0\rangle = \sum_{i \neq 0} \frac{\langle \psi_i | \frac{\partial \mathcal{H}}{\partial \alpha_x} | \psi_0 \rangle}{E_0 - E_i} |\psi_i\rangle. \tag{27}$$

Higher-order derivatives are simply obtained by repeated differentiation.

For bound-state observables, the computational overhead in terms of wall time is slightly larger than for two-body scattering since we must compute all eigenvalues and eigenvectors of $\mathcal{H}$. The calculation of all first and second derivatives for all 26 LECs at NNLO for the $A = 3$ observables is approximately 20 times slower than just calculating the central values.

G. Uncertainty quantification

We employ well-known methods from statistical regression analysis to study the sensitivities and quantify the uncertainties at the optimum $\chi^2(\boldsymbol{\alpha}_\star)$ (see, e.g., Dobaczewski *et al.* [79]). The $N_\alpha \times N_\alpha$ covariance matrix $\mathrm{Cov}(\boldsymbol{\alpha}_\star)$ defines the permissible variations $\Delta\boldsymbol{\alpha}$ in the LECs that maintain an objective function value such that

$$\chi^2(\boldsymbol{\alpha}_\star + \Delta\boldsymbol{\alpha}) - \chi^2(\boldsymbol{\alpha}_\star) \leq T, \tag{28}$$

where T is some chosen tolerance. We can assume rather small variations $\Delta\boldsymbol{\alpha}$ and therefore truncate a Taylor expansion of the objective function at the second order,

$$\chi^2(\boldsymbol{\alpha}_\star + \Delta\boldsymbol{\alpha}) - \chi^2(\boldsymbol{\alpha}_\star) \approx \frac{1}{2}(\Delta\boldsymbol{\alpha})^T \mathbf{H} (\Delta\boldsymbol{\alpha}),$$
$$\text{where } H_{ij} = \left.\frac{\partial^2 \chi^2(\boldsymbol{\alpha})}{\partial\alpha_i \partial\alpha_j}\right|_{\boldsymbol{\alpha}=\boldsymbol{\alpha}_\star} \tag{29}$$

are matrix elements of the Hessian $\mathbf{H}$. This should be positive definite. It can be decomposed into $\mathbf{H} = \mathbf{U}\mathbf{D}\mathbf{U}^T$, where the columns of $\mathbf{U}$ are the eigenvectors of $\mathbf{H}$ and $\mathbf{D}$ is a diagonal matrix with the eigenvalues of $\mathbf{H}$. Defining $\mathbf{x} \equiv \mathbf{U}^T(\Delta\boldsymbol{\alpha})$, Eq. (28) becomes

$$\frac{1}{2}\mathbf{x}^T \mathbf{D} \mathbf{x} = \frac{1}{2}\sum_{i=1}^{N_\alpha} x_i^2 D_{ii} \leq T. \tag{30}$$

The N_α parameters $\mathbf{x}$ can be viewed as "rotated" LECs. They are very convenient since they are independent of each other, which simplifies the previous equation and gives

$$\frac{1}{2} x_i^2 D_{ii} \leq T_1 \quad \forall\ i, \tag{31}$$

where T_1 is the limit to use when considering only variations in one parameter and keeping the others fixed. If $\chi^2(\boldsymbol{\alpha})$ follows a chi-squared distribution, then $x_i^2 D_{\chi^2,ii}/2$ will also follow a chi-squared distribution with 1 degree of freedom, meaning that the 1σ confidence level is given by $T_1 = 1$, and $x_i \sim \mathcal{N}(0, 2/D_{\chi^2,ii})$. In practice, $\chi^2(\boldsymbol{\alpha}_\star)$ will only be an approximate chi-squared distribution, which modifies T_1 slightly. Here, we set $T_1 = \chi^2(\boldsymbol{\alpha}_\star)/N_{\mathrm{dof}}$, which corresponds to a rescaling of the $\chi^2(\boldsymbol{\alpha}_\star)$ function [79],

$$\chi^2_{\mathrm{scaled}}(\boldsymbol{\alpha}) \equiv \chi^2(\boldsymbol{\alpha}) \frac{N_{\mathrm{dof}}}{\chi^2(\boldsymbol{\alpha}_\star)}. \tag{32}$$

The covariance matrix is then given by

$$\mathrm{Cov}(\boldsymbol{\alpha}_\star) = 2\frac{\chi^2(\boldsymbol{\alpha}_\star)}{N_{\mathrm{dof}}} \mathbf{H}^{-1} \equiv \mathbf{U}\boldsymbol{\Sigma}\mathbf{U}^T, \tag{33}$$

where $\boldsymbol{\Sigma}$ is the diagonal matrix with the vector of variances, $\boldsymbol{\sigma}^2$, of the rotated LECs, on the diagonal. Since T_1 only affects Cov with a constant factor, correlations remain invariant under changes in T_1.

1. Error propagation

Starting from the covariance matrix $\mathrm{Cov}(\boldsymbol{\alpha}_\star)$, we can propagate the statistical uncertainties in the LECs to any observable $\mathcal{O}_A$ and compute the linear correlation coefficient between any two observables $\mathcal{O}_A$ and $\mathcal{O}_B$. To this aim, it is most convenient to use the rotated and independent LEC representation $\mathbf{x}$ defined above. Each LEC x_i is normally distributed with zero mean. Next, we use a quadratic approximation of the observable $\mathcal{O}_A$,

$$\begin{aligned}
&\mathcal{O}_A(\boldsymbol{\alpha}_\star + \Delta\boldsymbol{\alpha}) - \mathcal{O}_A(\boldsymbol{\alpha}_\star) \\
&\quad \approx (\Delta\boldsymbol{\alpha})^T \mathbf{J}_A + \frac{1}{2}(\Delta\boldsymbol{\alpha})^T \mathbf{H}_A (\Delta\boldsymbol{\alpha}) \\
&\quad = \mathbf{x}^T U^T \mathbf{J}_A + \frac{1}{2}\mathbf{x}^T U^T \mathbf{H}_A U \mathbf{x} \\
&\quad \equiv \mathbf{x}^T \tilde{\mathbf{J}}_A + \frac{1}{2}\mathbf{x}^T \tilde{\mathbf{H}}_A \mathbf{x},
\end{aligned} \tag{34}$$

where $\mathbf{J}_A$ is the Jacobian vector of partial derivatives, $J_{A,i} = (\partial\mathcal{O}_A/\partial\alpha_i)$, $\mathbf{H}_A$ is the corresponding Hessian

matrix, and the tilde notation in the last line indicates the similarly rotated Jacobian and Hessian. The corresponding statistical expectation value $\mathbb{E}(\cdot)$ is given by

$$\mathbb{E}[\mathcal{O}_A(\boldsymbol{\alpha})] \approx \mathcal{O}_A(\boldsymbol{\alpha}_\star) + \frac{1}{2}\sum_{ij}^{N_\alpha} \tilde{H}_{A,ij}\mathbb{E}[x_i x_j] = \mathcal{O}_A(\boldsymbol{\alpha}_\star) + \frac{1}{2}(\boldsymbol{\sigma}^2)^T \mathrm{diag}(\tilde{\boldsymbol{H}}_A). \tag{35}$$

Finally, we define the covariance of $\mathcal{O}_A$ and $\mathcal{O}_B$ by

$$\begin{aligned}\mathrm{Cov}(A,B) &\equiv \mathbb{E}[(\mathcal{O}_A(\boldsymbol{\alpha}) - \mathbb{E}[\mathcal{O}_A(\boldsymbol{\alpha})]) \\ &\quad \times (\mathcal{O}_B(\boldsymbol{\alpha}) - \mathbb{E}[\mathcal{O}_B(\boldsymbol{\alpha})])] \\ &\approx \sum_{ijkl}^{N_\alpha} \mathbb{E}\left[\left(\tilde{J}_{A,i}x_i + \frac{1}{2}\tilde{H}_{A,ij}x_i x_j - \frac{1}{2}\tilde{H}_{A,ii}\sigma_i^2\right)\right. \\ &\quad \left.\times \left(\tilde{J}_{B,k}x_k + \frac{1}{2}\tilde{H}_{B,kl}x_k x_l - \frac{1}{2}\tilde{H}_{B,kk}\sigma_k^2\right)\right] \\ &= \tilde{\mathbf{J}}_A^T \Sigma \tilde{\mathbf{J}}_B + \frac{1}{2}(\boldsymbol{\sigma}^2)^T(\tilde{\mathbf{H}}_A \circ \tilde{\mathbf{H}}_B)\boldsymbol{\sigma}^2,\end{aligned} \tag{36}$$

where $\circ$ denotes the Hadamard product. The statistical uncertainty of an observable $\mathcal{O}_A$ is then given by $\sigma_A \equiv \sqrt{\mathrm{Cov}(A,A)}$. This approximation of the covariance is valid as long as the quadratic approximations (29) and (34) are valid and the normalized objective function can be assumed to follow a chi-squared distribution.

Using a linear approximation, the probability distribution for an observable $\mathcal{O}_A$ will follow the well-known Gaussian form. However, for the quadratic approximation, there is no such analytic expression. Instead, it is easy to reconstruct the probability distribution numerically by using Eq. (34) with a large sample of parameter sets.

III. RESULTS

In this section, we discuss our results from the optimization of χEFT at LO, NLO, and NNLO (Sec. III A), the subsequent error propagation (Sec. III B), as well as an expanded discussion on the implications and advantages of a simultaneous optimization protocol (Sec. III C.) In particular, we discuss the important consequences of correlations between the LECs in the case of simultaneous versus separate optimization strategies.

A. Optimization

With all the necessary tools in place, we can perform the fits to experimental data. For all cases, we implicitly assume that the LECs are of natural size [39] by choosing starting points in this region of the parameter space. We did not, in any other way, force the LECs to be natural. A possible problem in multiparameter optimization is the existence of several local minima. At LO, with just two parameters, there is only one minimum. However, at NLO we find four local minima. They correspond to combinations of two optima in the ${}^1S_0$ channel and two optima in the coupled ${}^3S_1 - {}^3D_1$ channel. As shown in Table III, all four combinations describe scattering data and the deuteron properties equally well, thus making them indistinguishable from this point of view. Furthermore, a similar set of minima exists at NNLO when fitting the πN and NN data separately.

A theoretical argument can provide partial guidance in the choice between these parameter sets. The nuclear interaction will have an approximate Wigner SU(4) symmetry [90] due to the large scattering lengths in the S waves, which implies $\tilde{C}_{{}^1S_0} \approx \tilde{C}_{{}^3S_1}$. This approximate constraint rules out the second and third of the four candidate LO and NLO minima in Table III. Furthermore, we might argue that the fourth minimum (NLO-4 and NNLO-4, respectively) is the physical one since its $\tilde{C}$ LECs most resemble the values obtained at LO. This is not a strong justification since LECs are allowed to vary between orders. In the end, it does turn out that both NLO-4 and NNLO-4 are indeed close to the single minimum that exists in the simultaneous NNLO optimization.

A much more interesting difference between the four minima occurs in the few-nucleon sector. It turns out that minima 1–3 give significant underbinding of the triton. Since the measured ground-state energy is -8.48 MeV, these results imply that three-nucleon forces, which appear at NNLO, would have to contribute 5–6 MeV of the missing binding energy. These differences are smaller for the NLO-4 and NNLO-4 minima, and they most likely represent the

TABLE III. Comparison of different minima at various chiral orders. NN-LECs are optimized using only NN scattering data (at NNLO, the πN LECs are fixed). The minima are equally good for $A = 2$ observables but differ significantly in $A = 3$ bound-state properties, calculated here without a three-body force. The last row corresponds to parameters and results (with NN forces only) of the simultaneously optimized NNLOsim interaction. The $\tilde{C}$ LECs are in units of 10^4 GeV^{-2}. The scattering χ^2/N_{dof} shown are for data up to 125 MeV without model errors included. $E^{(\mathrm{exp})\,({}^3\mathrm{H})} \approx -8.48$ MeV. Energies are in MeV.

	$\tilde{C}^{(np)}_{{}^1S_0}$	$\tilde{C}_{{}^3S_1}$	χ^2/N_{dof}	$E({}^2\mathrm{H})$	$E({}^3\mathrm{H})$
LOsep	−0.11	−0.072	350	−2.21	−11.4
NLO-1	+0.81	+0.69	14	−2.17	−3.03
NLO-2	+0.81	−0.17	14	−2.16	−3.30
NLO-3	−0.15	+0.68	14	−2.17	−2.92
NLO-4	−0.15	−0.17	14	−2.16	−8.22
NNLO-1	+0.49	+0.53	2.4	−2.19	−3.64
NNLO-2	+0.49	−0.17	2.4	−2.21	−3.71
NNLO-3	−0.15	+0.53	2.4	−2.19	−3.23
NNLO-4	−0.15	−0.17	2.4	−2.22	−8.21
NNLOsim	−0.15	−0.17	1.7	−2.22	−8.54

physical minima. This is also more in line with the power-counting arguments that the three-nucleon force should be weaker than the two-nucleon force (see, e.g., Ref. [91]). Furthermore, with the subsequent addition of the NNN terms at NNLO (as is done in the sequential optimization strategy), it turns out that only the NNLO-4 minimum allows us to reproduce all $A = 3$ observables within 1 standard deviation. For these reasons, NLO-4 and NNLO-4 define the NN-only parts of the NLOsep and NNLOsep potentials, respectively.

The values for the LECs of our optimized potentials at LO, NLO, and NNLO are tabulated in Ref. [92] together with their estimated statistical uncertainties. The statistical uncertainty of the ith LEC, i.e., $\sqrt{\mathrm{Cov}(\boldsymbol{\alpha}_*)_{ii}}$, is a measure of how much this particular parameter can change while maintaining a good description of the fitted data, as detailed in Sec. II G. In other words, the uncertainty for a given LEC represents its maximal variation while assuming that all other LECs are fixed at the χ^2 minimum. Note, however, that the LECs really cannot be varied independently of each other because of mutual correlations. A full error analysis requires a complete covariance matrix, as we demonstrate below.

The appearance of NNN diagrams and subleading terms from the πN sector does not occur until NNLO in our chiral expansion. This implies small differences between the separately and simultaneously optimized interactions at lower orders. The deuteron properties are included in the optimization of LOsim and NLOsim but not in LOsep and NLOsep. We find that the statistical χ^2 values (not including the model errors) with respect to NN scattering data are almost identical for LOsim and LOsep, and so are the values of the LECs. The small value of $\sigma_{\mathrm{exp+method}}$ for the deuteron binding energy constrains the statistical error for $\tilde{C}_{^3S_1}$ in LOsim correspondingly. For the contact potential at NLO, there are three LECs that operate in the deuteron channel, more than in any other NN partial wave. The presence of mutual correlations cannot be neglected. This explains why the individual statistical errors for the LECs in NLOsim and NLOsep in this channel are similar and larger than at LO. The covariances will also impact the value for the forward error in the deuteron binding energy, discussed further in Sec. III B.

We find that the description of the pp scattering data is not influenced much by the inclusion of the deuteron in the optimization, while the agreement with np data is notably worse above 35 MeV. At this order, it is mainly the $\tilde{C}_{^3S_1}$ and $C_{^1P_1}$ LECs that have changed (see Ref. [92]), which only affects np scattering.

As previously mentioned, the χEFT interaction becomes significantly more involved at NNLO as NNN and subleading πN terms enter at that order. The simultaneous optimization of all data listed in Table I leads to the construction of the NNLOsim interaction. The consequences of the simultaneous approach are dramatic. First of all, we find a single optimum, as this strategy eliminates all but one of the local minima that were obtained in the sequential optimization. Moreover, a possible concern turns out to be unwarranted: An improved overall description of scattering data does not deteriorate the description of different subsets. In fact, the result is quite the opposite. With the simultaneous-optimization strategy, we find that the description of the pp scattering data is actually significantly improved. For scattering energies $T_{\mathrm{lab}} \leq 290$ MeV, the statistical $\chi^2_{(pp)}/N_{\mathrm{dof}} = 9.1$ for NNLOsim compared to $\chi^2_{(pp)}/N_{\mathrm{dof}} = 26$ for NNLOsep, not including the model error. At the same time, the χ^2 for np scattering and πN scattering are similar for the two potentials. Measured np scattering cross sections are characterized by larger uncertainties, and it is therefore not surprising that these data remain well described. However, it is noteworthy that the NNLOsim potential reaches a better description of the NN data while maintaining a description of the πN data that is comparable to the one of NNLOsep. Keep in mind that NNLOsep is separately optimized to the πN scattering data. In the simultaneous optimization protocol, we are effectively introducing additional constraints on the c_i LECs via the NN data set. One might be concerned that the short-range NN physics would impact and worsen the description of the long-range pion physics. It is not unlikely that we would have seen such unphysical effects if the πN database was more comprehensive. The existing πN data do not constrain all directions in the πN LEC parameter space, which allows for large variations in the parameter values and a better description of the pp scattering data with NNLOsim. The χ^2/N_{dof} for NN and πN scattering up to different $T_{\mathrm{lab}}^{\mathrm{max}}$ are presented in Fig. 5.

The predominant advantage of the simultaneous optimization is the correct treatment of correlations. Although the uncertainties of the LECs presented in Ref. [92] are similar for NNLOsep and NNLOsim, the propagated statistical errors of observables can be several orders of magnitude larger for NNLOsep because of missing correlations (see Sec. III B). To visualize the correlations between all LECs, we plot the linear correlation matrix in Fig. 6. The linear correlation between two LECs, or any observables A and B, indicates their linear relationship and is defined as the normalized covariance, $\mathrm{Cov}(A,B)/(\sigma_A\sigma_B)$. This quantity assumes values between -1 (fully anticorrelated) and $+1$ (fully correlated). A positive (negative) value for the correlation indicates that a larger value for A most likely requires a larger (smaller) value for B. The correlation coefficients between LECs that belong to different objective functions are zero. For NNLOsep, this implies that the correlation matrix is block diagonal in terms of the πN, NN, and NNN sectors. For NNLOsim, however, such interblock correlations are revealed. In addition, we observe an increase of the correlations within each group. This can be traced to the fact that the πN LECs, c_1, c_3, and c_4, occur in the description of NN, πN, and

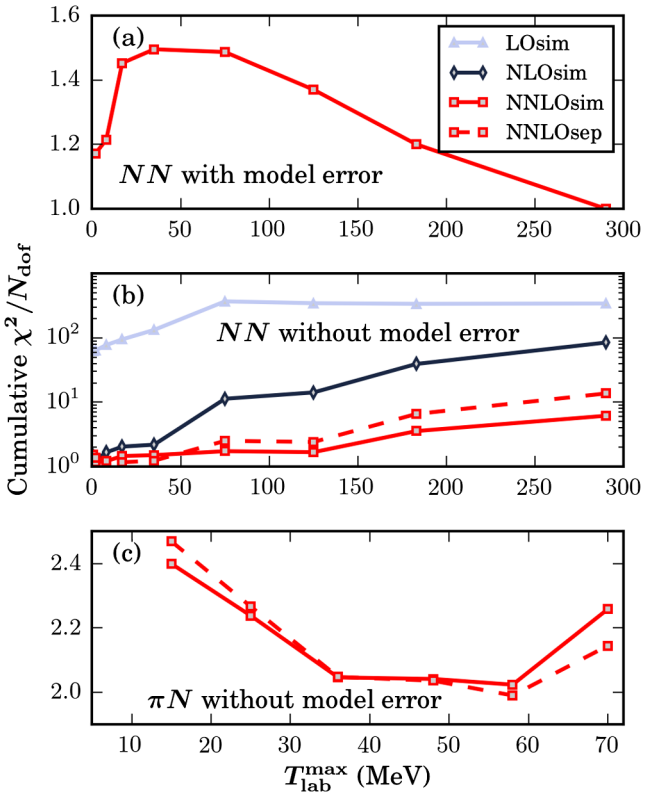

FIG. 5. (a) Cumulative $\chi^2/N_{\rm dof}$ for NN scattering data including the model error (see Sec. II E). Note that the amplitude of the model error is chosen so that $\chi^2/N_{\rm dof} = 1$ when all data up to $T_{\rm lab} = 290$ MeV are included. (b,c) Cumulative $\chi^2/N_{\rm dof}$ without the model error for NN and πN scattering data, respectively.

NNN data. The failure to capture these correlations within the sequential optimization approach, such as with the NNLOsep potential, will induce very large propagated statistical errors. In conclusion, simultaneous optimization is key for a realistic forward propagation of parametric uncertainties.

B. Error propagation

Statistical errors and covariances between computed observables are calculated under the assumption that each observable depends quadratically on the LECs in the vicinity of the minimum [see Eq. (34)]. Our estimate of the statistical uncertainty, σ_A, of an observable $\mathcal{O}_A$ rests on this assumption, which also explains why we have asymmetric error bars. We have performed extensive Monte Carlo samplings to verify the validity and necessity of using the second-order approximation. A linear truncation is more common. In particular, we compare the probability density function for various observables obtained from (i) Monte Carlo samplings of the multivariate Gaussian spanned by the covariance matrix, (ii) the quadratic approximation, and (iii) the linear approximation of Eq. (34). The Monte Carlo calculations use 10^5 sets of normally distributed LEC vectors.

The probability distributions for the scattering lengths a_{pp}^C and $a_{nn}^{\rm N}$ for the potentials NNLOsep and NNLOsim are shown in Fig. 7. Note that these results are predictions since the scattering lengths are not included in the objective function at NNLO. The statistical errors for a_{pp}^C and $a_{nn}^{\rm N}$

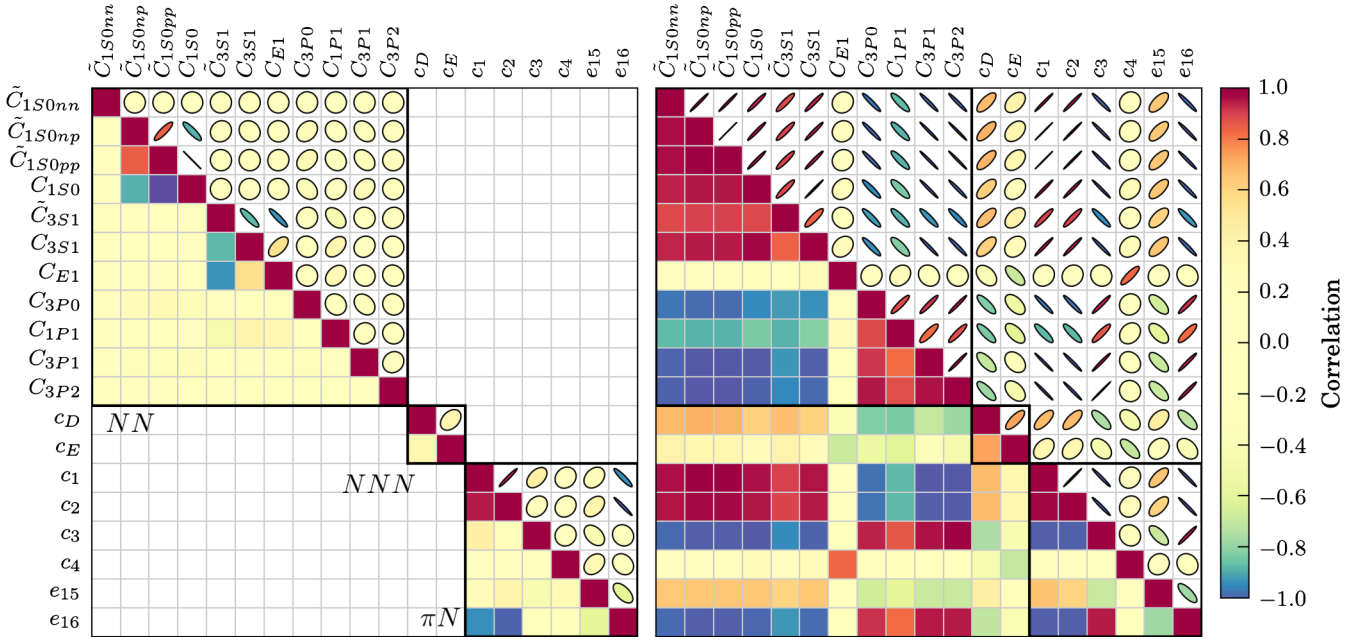

FIG. 6. Graphical representation of the linear correlation matrix for NNLOsep (left panel) and NNLOsim (right panel) including selected LECs. The separately optimized NNLOsep potential does not probe the statistical correlation between LECs entering different optimization stages. It is striking that there are almost no correlations for the NNLOsep potential, while for the NNLOsim potential the situation is quite the opposite.

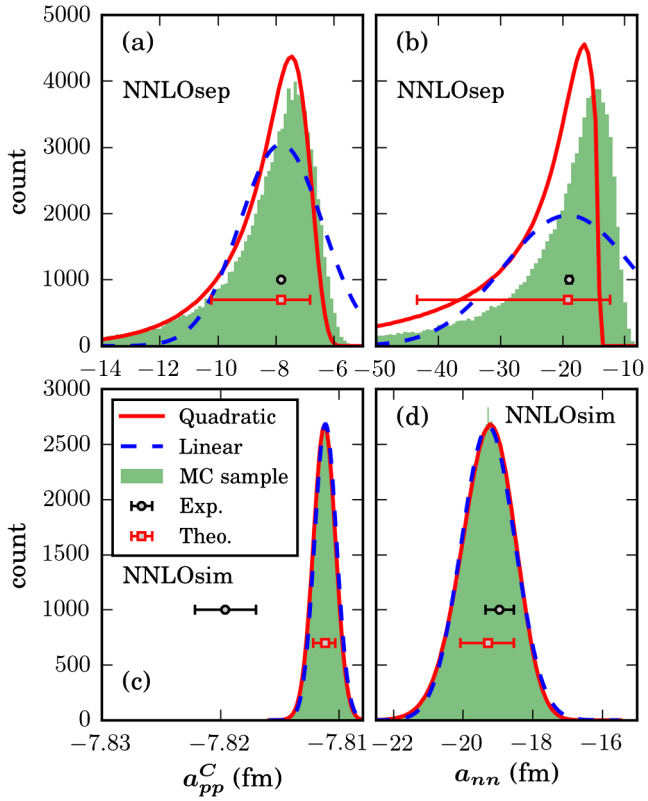

FIG. 7. Histograms (filled green area) for the sampled probability distribution of the nn (b,d) and pp (a,c) scattering lengths (including Coulomb) using the NNLO potentials: NNLOsep (a,b) and NNLOsim (c,d). The dashed (solid) lines show error estimates from the sample assuming that the scattering length depends linearly (quadratically) on the fitting parameters. The final theory result (red square) from Eq. (34) agrees well with the sampled distribution.

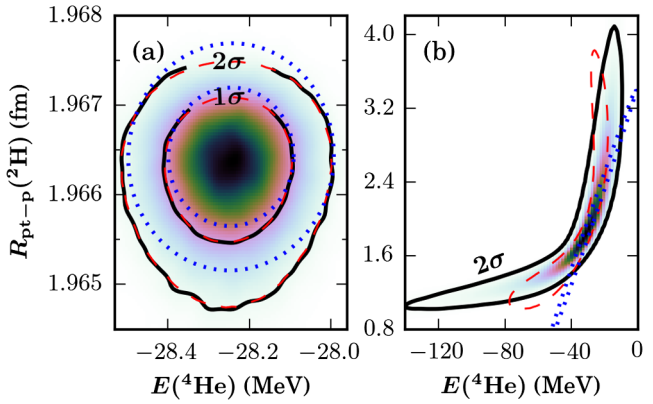

FIG. 8. Joint statistical probability distribution for $E(^4\mathrm{He})$ and $r_{\mathrm{pt-p}}(^2\mathrm{H})$ for (a) NNLOsim and (b) NNLOsep obtained in a Monte Carlo sampling ($N_{\mathrm{sample}} = 10^5$) as described in the text. Contour lines for this distribution are shown as black solid lines, while blue dotted (red dashed) contours are obtained assuming a linear (quadratic) dependence on the LECs for the observables.

obtained in the Monte Carlo calculations with the NNLOsim potential are small and well reproduced already by the corresponding linear approximation, as expected. With NNLOsep, the errors are much larger and require at least a quadratic approximation for the forward error. The uncertainties of the ERE parameters differ quite a lot between these two potentials. It is important to remember that for the NNLOsim potential, all LECs are constrained by πN, NN, as well as NNN data. Hence, in the error analysis, the LECs that fulfill $\chi^2_{\mathrm{scaled}}(\vec{p}) \approx N_{\mathrm{dof}}$ will provide a reasonable description of most scattering data. The πN LECs for NNLOsep, on the other hand, are constrained only by the πN data, and the missing statistical correlations allow for wide permissible ranges for the NN scattering lengths.

It is possible to explore correlations between any pair of observables by looking at joint probability distributions. As an example, we plot the statistical distribution of binding energies of ^{4}He and corresponding radii of the deuteron for the NNLO potentials in Fig. 8. The contour lines indicate the regions that encompass 68% (1σ) and 95% (2σ) of the probability density. It is remarkable that the quadratic approximation (dashed lines) reproduces even the fine details of the full calculation (solid lines) for the NNLOsim interaction. Again, the magnitude of variations is strikingly large for NNLOsep, but the quadratic approximation does rather well in reproducing them. In particular, we see a large improvement when going from a linear (dotted lines) to a quadratic dependence on the LECs. This even captures the departure from the standard first-order ellipse.

We present final results for bound-state observables in few-body systems ($A = 2$–4), as well as ERE parameters, in Table IV for the LO, NLO, and NNLO potentials. Observables that were part of the respective objective function are indicated by a regular emphasis, while entries with a bold emphasis are predictions. Note that the errors that are given in this table do not include a model error from the χEFT truncation, only the propagated statistical uncertainties as described in Sec. II G. It is therefore difficult to make strong conclusions regarding the order-by-order convergence, but we certainly observe improved predictions when going to higher orders. Note that LO results, in general, are characterized by small statistical uncertainties since very little freedom is allowed with just two parameters. At NNLO, we observe large statistical errors in the predictions following the sequential approach; e.g., with NNLOsep, the statistical error for $E(^4\mathrm{He})$ is more than 10 MeV.

Energies and radii of few-nucleon systems are well reproduced by NNLOsim as shown in Table IV, with the deuteron radius being the possible exception. This can be traced back to omitted relativistic effects. For the deuteron, Δr^2 has been estimated to be of the size 0.013 fm^2 [94] and 0.016 fm^2 [95].

We have also extracted correlations between other observables in the few-nucleon sector. As expected, for both

TABLE IV. Statistical uncertainties propagated from the NN, NNN, and πN LECs to the ground-state energies (in MeV) and radii (in fm) for $A \leq 4$ nuclei, the deuteron D-state probability $D(^2\mathrm{H})$ (in percent) and quadrupole moment $Q(^2\mathrm{H})$ (in e fm^2) and effective-range observables for the $^1S_0$ channel (in fm). The bold emphasis indicates that the corresponding result is a prediction. Asymmetrical errors are due to the quadratic dependence of the observables on the LECs. The error bars on the experimental values for bound-state observables include both experimental and method uncertainties as detailed in Table II.

	LOsep	NLOsep	NNLOsep	LOsim	NLOsim	NNLOsim	Experimental	Reference
$E(^2\mathrm{H})$	$\mathbf{-2.211(15)}$	$\mathbf{-2.163^{(+9)}_{(-16)}}$	$\mathbf{-2.2^{(+12)}_{(-25)}}$	-2.223	$-2.224^{(+1)}_{(-6)}$	$-2.224^{(+0)}_{(-1)}$	-2.225	Table II
$E(^3\mathrm{H})$	$\mathbf{-11.40(4)}$	$\mathbf{-8.220^{(+32)}_{(-49)}}$	$-8.5^{(+31)}_{(-64)}$	$\mathbf{-11.43}$	$\mathbf{-8.268^{(+26)}_{(-38)}}$	$-8.482^{(+26)}_{(-30)}$	$-8.482(28)$	Table II
$E(^3\mathrm{He})$	$\mathbf{-10.39(4)}$	$\mathbf{-7.474^{(+29)}_{(-45)}}$	$-7.7^{(+30)}_{(-62)}$	$\mathbf{-10.43}$	$\mathbf{-7.528^{(+20)}_{(-31)}}$	$-7.717^{(+17)}_{(-21)}$	$-7.718(19)$	Table II
$E(^4\mathrm{He})$	$\mathbf{-40.27(13)}$	$\mathbf{-27.56^{(+14)}_{(-18)}}$	$\mathbf{-28^{(+8)}_{(-18)}}$	$\mathbf{-40.38(1)}$	$\mathbf{-27.44^{(+13)}_{(-15)}}$	$\mathbf{-28.24^{(+9)}_{(-11)}}$	$-28.30(11)$	Table II
$r_{\text{pt-p}}(^2\mathrm{H})$	$\mathbf{+1.916(5)}$	$\mathbf{+1.977^{(+2)}_{(-5)}}$	$\mathbf{+1.97^{(+67)}_{(-52)}}$	$+1.912$	$+1.972^{(+0)}_{(-2)}$	$+1.966^{(+0)}_{(-1)}$	$+1.976(1)$	Table II
$r_{\text{pt-p}}(^3\mathrm{H})$	$\mathbf{+1.293(2)}$	$\mathbf{+1.596(3)}$	$+1.58^{(+22)}_{(-30)}$	$\mathbf{+1.292}$	$\mathbf{+1.614^{(+2)}_{(-3)}}$	$+1.581(2)$	$+1.587(41)$	Table II
$r_{\text{pt-p}}(^3\mathrm{He})$	$\mathbf{+1.370(2)}$	$\mathbf{+1.778^{(+3)}_{(-4)}}$	$+1.76^{(+23)}_{(-33)}$	$\mathbf{+1.368}$	$\mathbf{+1.791(3)}$	$+1.761(2)$	$+1.766(13)$	Table II
$r_{\text{pt-p}}(^4\mathrm{He})$	$\mathbf{+1.081(1)}$	$\mathbf{+1.459(4)}$	$\mathbf{+1.44^{(+15)}_{(-28)}}$	$\mathbf{+1.080}$	$\mathbf{+1.482(3)}$	$\mathbf{+1.445(3)}$	$+1.455(7)$	Table II
$E_A^1(^3\mathrm{H})$	⋯	⋯	$+0.685^{(+22)}_{(-50)}$	⋯	⋯	$+0.6848(11)$	$+0.6848(11)$	Table II
$D(^2\mathrm{H})$	$\mathbf{+7.794(17)}$	$\mathbf{+2.942^{(+85)}_{(-81)}}$	$\mathbf{+3.9^{(+18)}_{(-12)}}$	$\mathbf{+7.807}$	$\mathbf{+2.876^{(+85)}_{(-82)}}$	$\mathbf{+3.381^{(+46)}_{(-45)}}$	⋯	
$Q(^2\mathrm{H})$	$\mathbf{+0.3035(7)}$	$\mathbf{+0.2602^{(+16)}_{(-20)}}$	$\mathbf{+0.270^{(+60)}_{(-63)}}$	$+0.3030$	$+0.2589^{(+17)}_{(-19)}$	$+0.2623(8)$	$+0.270(11)$	Table II
a_{nn}^{N}	$\mathbf{-26.04(5)}$	$-18.95^{(+44)}_{(-47)}$	$\mathbf{-19^{(+7)}_{(-24)}}$	$\mathbf{-26.04(8)}$	$-18.95^{(+38)}_{(-41)}$	$\mathbf{-19.28^{(+74)}_{(-80)}}$	$-18.95(40)$	[18]
a_{np}^{N}	$\mathbf{-25.58(5)}$	$\mathbf{-23.37^{(+16)}_{(-19)}}$	$\mathbf{-24^{(+11)}_{(-44)}}$	$\mathbf{-25.58(8)}$	$\mathbf{-23.60^{(+10)}_{(-13)}}$	$\mathbf{-23.83(11)}$	-23.71	[93]
a_{pp}^{C}	$\mathbf{-7.579(4)}$	$\mathbf{-7.799^{(+1)}_{(-3)}}$	$\mathbf{-7.8^{(+10)}_{(-24)}}$	$\mathbf{-7.579(6)}$	$\mathbf{-7.799^{(+1)}_{(-3)}}$	$\mathbf{-7.811(1)}$	$-7.820(3)$	[62]
r_{nn}^{N}	$\mathbf{+1.697}$	$+2.752(7)$	$\mathbf{+2.85^{(+21)}_{(-34)}}$	$\mathbf{+1.697(1)}$	$+2.752^{(+7)}_{(-8)}$	$\mathbf{+2.793(14)}$	$+2.75(11)$	[18]
r_{np}^{N}	$\mathbf{+1.700}$	$\mathbf{+2.650^{(+3)}_{(-4)}}$	$\mathbf{+2.74^{(+20)}_{(-33)}}$	$\mathbf{+1.700(1)}$	$\mathbf{+2.648(3)}$	$\mathbf{+2.686(2)}$	$+2.750(62)$	[93]
r_{pp}^{C}	$\mathbf{+1.812}$	$\mathbf{+2.704(3)}$	$\mathbf{+2.81^{(+18)}_{(-30)}}$	$\mathbf{+1.812(1)}$	$\mathbf{+2.704(3)}$	$\mathbf{+2.758(2)}$	$+2.790(14)$	[62]

NNLOsep and NNLOsim, there exists a significant correlation between the D-state probability and the quadrupole moment of the deuteron. More interestingly, at the present optima, the triton β-decay half-life does not correlate strongly with any other bound-state observable in Table IV. This corroborates the importance of using this observable to constrain nuclear forces, as was done already in Ref. [77].

Total uncertainties (statistical plus estimated model error from the χEFT truncation) are shown for scattering observables in Fig. 9. The statistical errors are typically very small compared to the model error for the LOsim, NLOsim, and NNLOsim potentials [Figs. 9(b)–9(e)]. Clear signatures of an order-by-order convergence are seen in the NN scattering observables as illustrated by the np total cross section and the differential cross section that are shown in Figs. 9(b) and 9(c). The same convergence is not seen when using the sequentially optimized potentials as illustrated in Fig. 9(a). In this case, the statistical errors are of the same order of magnitude as the model errors, and the NNLO error band is even wider than the NLO band. Note that πN scattering is only described with the NNLOsep and NNLOsim interactions.

C. Optimization protocol

We have demonstrated that the statistical uncertainties of χEFT, if all correlations are accounted for, will induce rather small errors in the predictions of observables. This reflects the fact that most of the few-nucleon data are precise and diverse enough to constrain a statistically meaningful χEFT description of the nuclear interaction. Also, note that we only included experimentally observable data in the objective function.

The existence of strong correlations between the LECs requires a complete determination of the corresponding covariance matrix, not just the diagonal entries. For this, it is necessary to employ the so-called simultaneous optimization protocol. To further demonstrate this point, we carried out error propagations with NNLOsim while neglecting the off-diagonal correlations between the LECs. The statistical uncertainty of the binding energy in ^{4}He grew with a factor $\sim$90 compared with the fully informed model. Neglecting the statistical correlations will also obscure the desired convergence pattern of χEFT. Indeed, for the separately optimized

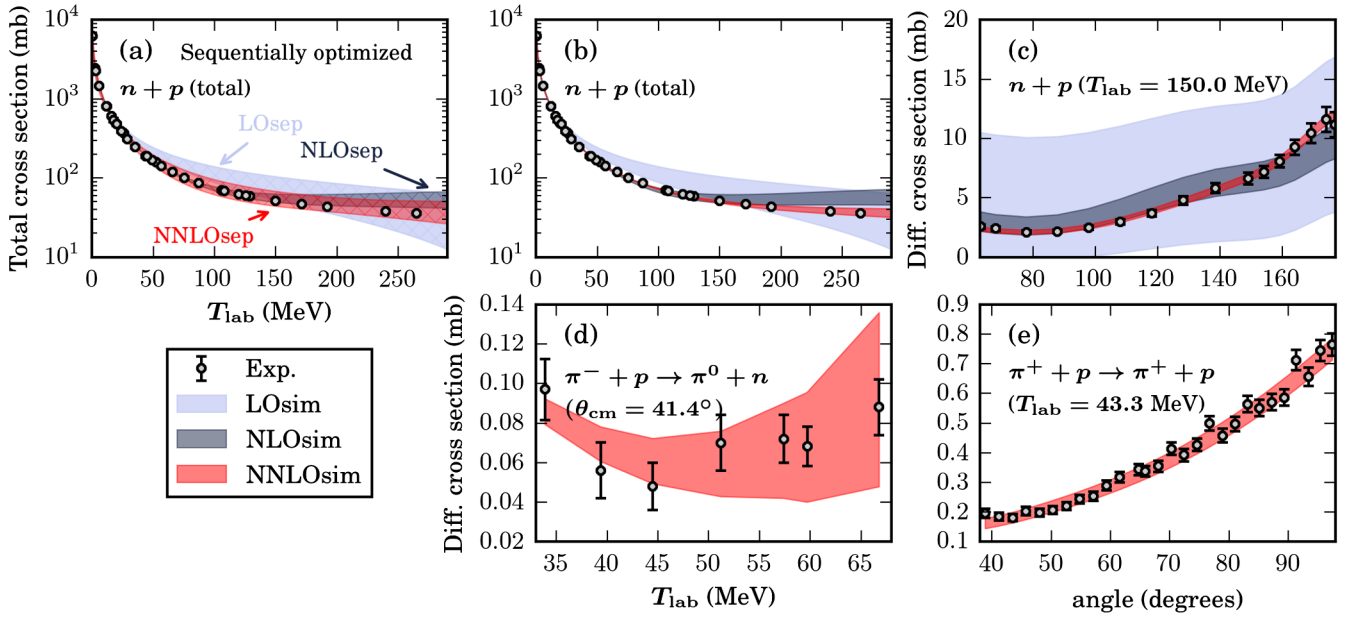

FIG. 9. Comparison between selected NN and πN experimental data sets and theoretical calculations for chiral interactions at LO, NLO, and NNLO. The bands indicate the total errors (statistical plus model errors). (a) np total cross section for the sequentially optimized interactions with no clear signature of convergence with increasing chiral order. All other results are for the simultaneously optimized interactions: LOsim, NLOsim, and NNLOsim. (b) np total cross section; (c) np differential cross section; (d) πN charge-exchange, differential cross section; (e) πN elastic, differential cross section.

potentials, there were no signs of convergence in the description of, e.g., np scattering data.

If the experimental database of πN scattering cross sections was complete, then it would be possible to separately constrain, with zero variances, the corresponding LECs. Only this scenario would render it unnecessary to include the πN scattering data in the simultaneous objective function. Implicitly, this scenario also assumes a perfect theory, i.e., that the employed χEFT can account for the dynamics of pionic interactions. Of course, reality lies somewhere in between, and a simultaneous optimization approach is preferable in the present situation. There exists ongoing efforts where the πN sector of χEFT is extrapolated and fitted separately in the unphysical kinematical region, where it exhibits a stronger curvature with respect to the data [96].

Overall, the importance of applying simultaneous optimization is most prominent at higher chiral orders since the subleading πN LECs enter first at NNLO. In fact, the separately optimized NNLOsep potential contains a large systematic uncertainty by construction. We find that the scaling factor for the NN scattering model error, C_{NN}, decreases from 1.6 to 1.0 $\mathrm{mb}^{1/2}$ when going from NNLOsep to the simultaneously optimized NNLOsim. This implies that the separate, or sequential, optimization protocol introduces additional artificial systematic errors not due to the chiral expansion but due to incorrectly fitted LECs. This scenario is avoided in a simultaneous optimization. The scaling factor for the πN scattering model error, $C_{\pi\mathrm{N}}$, remains at 3.6 $\mathrm{mb}^{1/2}$ for both NNLOsep and NNLOsim.

The size of the model error is determined such that the overall scattering χ^2/N_{dof} is unity, which means that it depends on the observables entering the optimization. We can explore the stability of our approach by reoptimizing NNLOsim with respect to different truncations of the input NN scattering data. To this end, we adjust the allowed $T_{\mathrm{lab}}^{\mathrm{max}}$ between 125 and 290 MeV in six steps. It turns out that our procedure for extracting the model error is very stable. The resulting normalization constants C_{NN} vary between 1.0 $\mathrm{mb}^{1/2}$ and 1.3 $\mathrm{mb}^{1/2}$ as shown in Fig. 10(a).

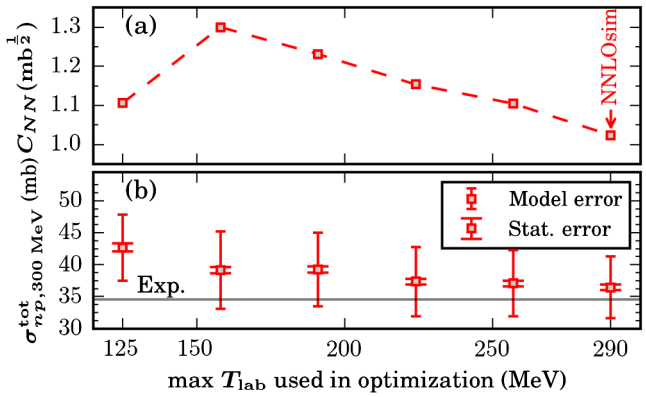

FIG. 10. Predictions for the different reoptimizations of NNLOsim. On the x axis is the maximum T_{lab} for the NN scattering data used in the optimization. (a) Model error amplitude (20) reoptimized so that $\chi^2/N_{\mathrm{dof}} = 1$ for the respective data subset. (b) Model prediction for the np total cross section at $T_{\mathrm{lab}} = 300$ MeV with error bars representing statistical and model errors for the different reoptimizations.

To see the corresponding effect on predicted observables, we consider the np total cross section at laboratory scattering energy $T_{\rm lab} = 300$ MeV. The model errors vary between 4.8 mb and 6.1 mb, and the calculated cross sections vary between 36.5 mb and 42.7 mb [see Fig. 10(b)]. The measured value is 34.563(174) mb [21,97]. We note that the size of the estimated model error is comparable with the variation in the predictions due to changing $T_{\rm lab}^{\rm max}$.

Throughout the analysis, the model error for scattering observables was assumed to scale with momentum p according to Eq. (20). However, the soft scale Q in χEFT is set by $\max\{p, m_\pi\}$, and it can be argued that the model error should be implemented as

$$\tilde{\sigma}_{\rm model,x}^{\rm (amp)} = C_{\rm x}\left(\frac{\max\{p, m_\pi\}}{\Lambda_\chi}\right)^{\nu_{\rm x}+1}. \tag{37}$$

It turns out that resolving these two momentum scales has a small impact on the estimated model errors. As an illustration, the predictions of the ^{4}He binding energy changes by just $\sim$20 keV (less than 0.1%). In fact, this effect is much smaller than the impact of changing the $T_{\rm lab}^{\rm max}$ cutoff in the experimental NN scattering database.

IV. EXTENDED ANALYSIS OF SYSTEMATIC UNCERTAINTIES

In nuclear physics, the theoretical uncertainties very often dominate over the experimental ones. In particular, this is true for the systematic error. Therefore, it is crucial to establish a credible program for assessing the error budget of any prediction or analysis of experimental information. Thus, we focus our attention on the convergence and missing physics in χEFT. In particular, we discuss consequences for predictions of bound-state observables in heavier nuclei such as ^{4}He and ^{16}O. It would be valuable to estimate the systematic uncertainty of predicted bound-state observables—due to the momentum-dependent χEFT uncertainty $\sigma_{\rm model}$ in Eq. (20). However, the explicit momentum dependence is integrated over when solving the nonrelativistic Schrödinger equation. Thus, a clear connection to the momentum expansion is lost.

As demonstrated already in Fig. 10, the variations in model predictions obtained from different truncations of the input data (including only NN scattering data with $T_{\rm lab} \leq T_{\rm lab}^{\rm max}$) are a good first approximation of the expected model uncertainty. To get a more complete picture of the systematic uncertainty, we now also vary the regulator cutoff parameter Λ in the range 450–600 MeV in steps of 25 MeV. For each combination of $T_{\rm lab}^{\rm max}$ and Λ, we perform a simultaneous optimization of the LECs, which results in a family of 42 NNLO interactions—i.e., 42 sets of LECs that each comes with statistical uncertainties. It is clear from Table V that the statistical uncertainties of the LECs are smaller than the overall shifts induced by varying $T_{\rm Lab}^{\rm max}$ and the cutoff Λ. All sets of LECs at LO, NLO, and NNLO that were obtained in this work are listed in Ref. [92]. Furthermore, each set is accompanied by its own covariance matrix, also available for download. In the following discussion, we use this family of potentials to estimate the systematic uncertainty.

TABLE V. Ranges of LEC values and maximum statistical uncertainties among all 42 simultaneously optimized NNLO potentials constructed in this work (see Sec. IV). The first two columns show the global variation of the LEC values, in terms of minimum and maximum values, due to changes in Λ and $T_{\rm Lab}^{\rm max}$. The third column shows the maximum statistical uncertainty of each LEC, which almost exclusively comes from the $\Lambda = 450$ MeV and $T_{\rm Lab}^{\rm max} = 125$ MeV NNLOsim potential. For a given LEC, the statistical uncertainty is rather similar for different potentials. $\tilde{C}_i$ are in units of 10^4 GeV^{-2}, C_i in units of 10^4 GeV^{-4}, c_D and c_E are dimensionless, while c_i, d_i, and e_i are in units of GeV^{-1}, GeV^{-2}, and GeV^{-3}, respectively.

LEC	Range	$\max(\sigma)$
$\tilde{C}_{^1S_0}^{(np)}$	$-0.1519 \ldots -0.1464$	± 0.0020
$\tilde{C}_{^1S_0}^{(pp)}$	$-0.1512 \ldots -0.1454$	± 0.0020
$\tilde{C}_{^1S_0}^{(nn)}$	$-0.1518 \ldots -0.1463$	± 0.0021
$C_{^1S_0}$	$2.4188 \ldots 2.5476$	± 0.0511
$\tilde{C}_{^3S_1}$	$-0.1807 \ldots -0.1348$	± 0.0032
$\tilde{C}_{^3S_1}$	$0.5037 \ldots 0.7396$	± 0.0521
C_{E_1}	$0.2792 \ldots 0.6574$	± 0.0253
$C_{^3P_0}$	$0.9924 \ldots 1.6343$	± 0.0428
$C_{^1P_1}$	$0.0618 \ldots 0.6635$	± 0.0438
$C_{^3P_1}$	$-0.9666 \ldots -0.4724$	± 0.0416
$C_{^3P_2}$	$-0.7941 \ldots -0.6324$	± 0.0327
c_D	$-0.5944 \ldots 0.8348$	± 0.0833
c_E	$-2.4019 \ldots -0.0893$	± 0.2282
c_1	$-0.8329 \ldots 0.2784$	± 0.3043
c_2	$2.7946 \ldots 5.3258$	± 1.0754
c_3	$-4.3601 \ldots -3.4474$	± 0.1506
c_4	$1.8999 \ldots 4.2353$	± 0.2179
$d_1 + d_2$	$4.4636 \ldots 5.4505$	± 0.1378
d_3	$-4.8549 \ldots -4.4583$	± 0.2302
d_5	$-0.2992 \ldots 0.0233$	± 0.1407
$d_{14} - d_{15}$	$-10.3220 \ldots -9.6902$	± 0.2820
e_{14}	$-0.3700 \ldots 0.9569$	± 0.9079
e_{15}	$-11.9223 \ldots -9.1307$	± 2.4962
e_{16}	$-0.6847 \ldots 7.4463$	± 4.2436
e_{17}	$0.9322 \ldots 1.4986$	± 1.8143
e_{18}	$-2.5068 \ldots 8.3777$	± 1.9022

First, we would like to emphasize that all sets of simultaneously optimized LECs provide an almost equally

good description of all $A \leq 4$ data. Some of the πN LECs display large variations, but the χ^2/N_{dof} (without model error) for the πN data is within 2.28(4) for all of these potentials. The subleading πN LECs become more positive when NN scattering data at higher energies are included, and c_1, in particular, carries a larger (relative) statistical uncertainty than the others. It is noteworthy that for a given $T_{\mathrm{Lab}}^{\mathrm{max}}$, and up to 1σ precision, the πN LECs exhibit Λ independence. The NNN LECs, c_D and c_E, tend to depend less on $T_{\mathrm{Lab}}^{\mathrm{max}}$ at larger values of Λ. However, they always remain natural. It is also interesting to note that the tensor contact C_{E_1} is insensitive to Λ variations but strongly dependent on the $T_{\mathrm{Lab}}^{\mathrm{max}}$ cut. It was shown in Fig. 6 that C_{E_1} and c_4 correlate strongly. This effect can already be expected from the structure of the underlying expression for the NNLO interaction.

To gauge the magnitude of model variations in heavier nuclei, we computed the binding energies of ^{4}He and ^{16}O by using the previously mentioned family of 42 NNLO potentials. The resulting binding energies for ^{4}He and ^{16}O, computed in the NCSM and CC, respectively, are shown in Fig. 11. The NCSM calculations were carried out in a HO model space with $N_{\mathrm{max}} = 20$ and $\hbar\omega = 36$ MeV. The CC calculations were carried out in the so-called Λ−CCSD(T) approximation [7] in 15 major oscillator shells with $\hbar\omega = 22$ MeV. The largest energy difference when going from 13 to 15 oscillator shells was 3.6 MeV (observed for $\Lambda = 600$ MeV). From the observed convergence of the correlation energy we estimate the uncertainty of excluded higher rank excitation clusters to ± 5 MeV. For our purposes, this provides well-enough converged results. The NNN force was truncated at the normal-ordered two-body level in the Hartree-Fock basis.

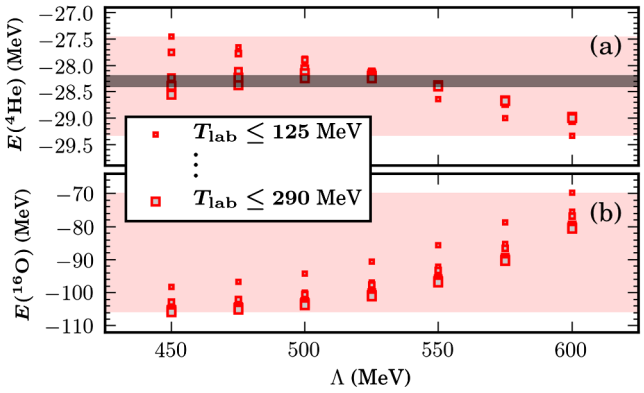

FIG. 11. Binding-energy predictions for (a) ^{4}He and (b) ^{16}O with the different reoptimizations of NNLOsim. On the x axis is the employed cutoff Λ. Vertically aligned red markers correspond to different $T_{\mathrm{Lab}}^{\mathrm{max}}$ for the NN scattering data used in the optimization. The experimental binding energies are $E(^4\mathrm{He}) \approx -28.30$ MeV, represented by a gray band in panel (a), and $E(^{16}\mathrm{O}) \approx -127.6$ MeV [98]. Statistical error bars on the theoretical results are smaller than the marker size on this energy scale.

The $E(^4\mathrm{He})$ predictions vary within about a 2-MeV range. For $E(^{16}\mathrm{O})$, this variation increases dramatically to about 35 MeV. Irrespective of the discrepancy with the measured value, the spread of the central values indicates the presence of a surprisingly large systematic error when extrapolating to heavier systems.

The statistical uncertainties remain small: tens of keV for ^{4}He and a few hundred keV for ^{16}O. These uncertainties are obtained from the quadratic approximation with the computed Jacobian and Hessian for ^{4}He, while a brute-force Monte Carlo simulation with 2.5×10^4 CC calculations was performed for ^{16}O. This massive set of CC calculations employed the singles and doubles approximation (CCSD) in nine major oscillator shells. We conclude that the statistical uncertainties of the predictions for $E(^4\mathrm{He})$ and $E(^{16}\mathrm{O})$ at NNLO are much smaller than the variations due to changing Λ or $T_{\mathrm{Lab}}^{\mathrm{max}}$. However, this is only true for simultaneously optimized potentials. For the separately optimized NNLO potential (NNLOsep), the statistical uncertainty of the $E(^4\mathrm{He})$ prediction is five times larger than the observed variations due to changing Λ and $T_{\mathrm{Lab}}^{\mathrm{max}}$.

V. OUTLOOK

The extended analysis of systematic uncertainties presented above suggests that large fluctuations are induced in heavier nuclei (see Fig. 11). Furthermore, while predictions for ^{4}He are accurate over a rather wide range of regulator parameters, the binding energy for ^{16}O turns out to be underestimated for the entire range used in this study. In fact, there is no overlap between the theoretical predictions and the experimental results, even though the former ones have large error bars.

Based on our findings, we recommend that continued efforts towards an *ab initio* framework based on χEFT should involve additional work in, at least, three different directions:

(1) Explore the alternative strategy of informing the model about low-energy many-body observables.
(2) Diversify and extend the statistical analysis and perform a sensitivity analysis of input data.
(3) Continue efforts towards higher orders of the chiral expansion, and possibly revisit the power counting.

Let us comment briefly on these research directions. The poor many-body scaling observed in Fig. 11 was pragmatically accounted for in the construction of the so-called $\mathrm{NNLO}_{\mathrm{sat}}$ potential presented in Ref. [35], where heavier nuclei were also included in the fit. The accuracy of many-body predictions was shown to be much improved, but the uncertainty analysis is much more difficult within such a strategy.

Second, to get a handle on possible bias in the statistical analysis due to the choice of statistical technique, it is important to apply different types of optimization and uncertainty quantification methods. Various choices exist,

such as, e.g., Lagrange multiplier analysis [99], Bayesian methods [100], or Gaussian process modeling [101,102]. In general, stochastic modeling with Monte Carlo simulations offers a straightforward and versatile approach. This tool is also indispensable for computing the posterior probabilities in Bayesian inference. The Monte Carlo results for $A \leq 4$ observables that were presented in this work consist of 10^5 sampling points over a multivariate Gaussian parameter space. With our current implementation, the computational cost for sampling all $A \leq 4$ observables presented in this work is very low—less than 8000 CPU hours. As such, the present work also shows great promise for future stochastic applications.

Furthermore, the computational framework that we have presented here, and our present implementation, is not limited to any particular type of regulator function or flavor of chiral expansion. Moreover, the handling of a larger number of LECs, as would be the consequence of working at a higher chiral order, should be relatively straightforward and we do not foresee any computational bottlenecks.

Finally, the magnitude of the systematic uncertainties that were observed in this work suggest the need to further explore and improve the theoretical underpinnings of the chiral expansion of the nuclear interaction.

ACKNOWLEDGMENTS

The authors thank D. Furnstahl, G. Hagen, M. Hjorth-Jensen, W. Nazarewicz, and T. Papenbrock for valuable comments and fruitful discussions. The research leading to these results has received funding from the European Research Council under the European Community's Seventh Framework Programme (FP7/2007-2013)/ERC Grant No. 240603 and the Swedish Foundation for International Cooperation in Research and Higher Education (STINT, Grant No. IG2012-5158). This material is based upon work supported by the U.S. Department of Energy, Office of Science, Office of Nuclear Physics under Grants No. DEFG02-96ER40963 (University of Tennessee) and No. DE-SC0008499 (NUCLEI SciDAC Collaboration) and under Contract No. DE-AC05-00OR22725 (Oak Ridge National Laboratory). The computations were performed on resources provided by the Swedish National Infrastructure for Computing at NSC, HPC2C, and C3SE. This research also used resources of the Oak Ridge Leadership Computing Facility located in the Oak Ridge National Laboratory. One of us (A. E.) wants to acknowledge the hospitality of Chalmers University of Technology where the implementation of Automatic Differentiation was performed, while the hospitality of Oslo University is acknowledged by B. C.

[1] A. T. Valderrama, J. Witteveen, M. Navarro, and J. Blom, *Uncertainty Propagation in Nerve Impulses Through the Action Potential Mechanism*, J. Math. Neurosci. **5**, 3 (2015).

[2] J. M. Murphy, D. M. H. Sexton, D. N. Barnett, G. S. Jones, M. J. Webb, M. Collins, and D. A. Stainforth, *Quantification of Modelling Uncertainties in a Large Ensemble of Climate Change Simulations*, Nature (London) **430**, 768 (2004).

[3] P. Angelikopoulos, C. Papadimitriou, and P. Koumoutsakos, *Bayesian Uncertainty Quantification and Propagation in Molecular Dynamics Simulations: A High Performance Computing Framework*, J. Chem. Phys. **137**, 144103 (2012).

[4] J. Erler, N. Birge, M. Kortelainen, W. Nazarewicz, E. Olsen, A. M. Perhac, and M. Stoitsov, *The Limits of the Nuclear Landscape*, Nature (London) **486**, 509 (2012).

[5] M. Cacciari and N. Houdeau, *Meaningful Characterisation of Perturbative Theoretical Uncertainties*, J. High Energy Phys. 11 (2011) 039.

[6] B. R. Barrett, P. Navrátil, and J. P. Vary, *Ab Initio No Core Shell Model*, Prog. Part. Nucl. Phys. **69**, 131 (2013).

[7] G. Hagen, T. Papenbrock, M. Hjorth-Jensen, and D. J. Dean, *Coupled-Cluster Computations of Atomic Nuclei*, Rep. Prog. Phys. **77**, 096302 (2014).

[8] S. C. Pieper and R. B. Wiringa, *Quantum Monte Carlo Calculations of Light Nuclei*, Annu. Rev. Nucl. Part. Sci. **51**, 53 (2001).

[9] D. Lee, *Lattice Simulations for Few- and Many-Body Systems*, Prog. Part. Nucl. Phys. **63**, 117 (2009).

[10] W. Leidemann and G. Orlandini, *Modern Ab Initio Approaches and Applications in Few-Nucleon Physics with* $a \geq 4$, Prog. Part. Nucl. Phys. **68**, 158 (2013).

[11] C. Romero-Redondo, S. Quaglioni, P. Navrátil, and G. Hupin, $^4\mathrm{He} + n + n$ *Continuum within an Ab Initio Framework*, Phys. Rev. Lett. **113**, 032503 (2014).

[12] A. Deltuva and A. C. Fonseca, *Proton-*^{3}H *Scattering Calculation: Elastic and Charge-Exchange Reactions up to 30 MeV*, Phys. Rev. C **91**, 034001 (2015).

[13] B. Mihaila and J. H. Heisenberg, *Microscopic Calculation of the Inclusive Electron Scattering Structure Function in* ^{16}O, Phys. Rev. Lett. **84**, 1403 (2000).

[14] T. A. Lähde, E. Epelbaum, H. Krebs, D. Lee, U.-G. Meißner, and G. Rupak, *Lattice Effective Field Theory for Medium-Mass Nuclei*, Phys. Lett. B **732**, 110 (2014).

[15] V. Somà, C. Barbieri, and T. Duguet, *Ab Initio Gorkov-Green's Function Calculations of Open-Shell Nuclei*, Phys. Rev. C **87**, 011303 (2013).

[16] H. Hergert, S. K. Bogner, S. Binder, A. Calci, J. Langhammer, R. Roth, and A. Schwenk, *In-Medium Similarity Renormalization Group with Chiral Two- Plus Three-Nucleon Interactions*, Phys. Rev. C **87**, 034307 (2013).

[17] E. Epelbaum, H.-W. Hammer, and U.-G. Meißner, *Modern Theory of Nuclear Forces*, Rev. Mod. Phys. **81**, 1773 (2009).

[18] R. Machleidt and D. R. Entem, *Chiral Effective Field Theory and Nuclear Forces*, Phys. Rep. **503**, 1 (2011).

[19] N. Barnea, L. Contessi, D. Gazit, F. Pederiva, and U. van Kolck, *Effective Field Theory for Lattice Nuclei*, Phys. Rev. Lett. **114**, 052501 (2015).

[20] V. G. J. Stoks, R. A. M. Klomp, M. C. M. Rentmeester, and J. J. de Swart, *Partial-Wave Analysis of All Nucleon-Nucleon Scattering Data below 350 MeV*, Phys. Rev. C **48**, 792 (1993).

[21] R. A. Arndt, I. I. Strakovsky, and R. L. Workman, *SAID, Scattering Analysis Interactive Dial-in Computer Facility, George Washington University (formerly Virginia Polytechnic Institute), solution SM99* (1999); for more information see, e.g., R. A. Arndt, I. I. Strakovsky, and R. L. Workman, Phys. Rev. C **50**, 2731 (1994).

[22] V. G. J. Stoks, R. A. M. Klomp, C. P. F. Terheggen, and J. J. de Swart, *Construction of High-Quality NN Potential Models*, Phys. Rev. C **49**, 2950 (1994).

[23] R. B. Wiringa, V. G. J. Stoks, and R. Schiavilla, *Accurate Nucleon-Nucleon Potential with Charge-Independence Breaking*, Phys. Rev. C **51**, 38 (1995).

[24] R. Machleidt, *High-Precision, Charge-Dependent Bonn Nucleon-Nucleon Potential*, Phys. Rev. C **63**, 024001 (2001).

[25] Steven C. Pieper, V. R. Pandharipande, R. B. Wiringa, and J. Carlson, *Realistic Models of Pion-Exchange Three-Nucleon Interactions*, Phys. Rev. C **64**, 014001 (2001).

[26] D. R. Entem and R. Machleidt, *Accurate Charge-Dependent Nucleon-Nucleon Potential at Fourth Order of Chiral Perturbation Theory*, Phys. Rev. C **68**, 041001 (2003).

[27] E. Epelbaum, W. Glöckle, and U.-G. Meißner, *The Two-Nucleon System at Next-to-Next-to-Next-to-Leading Order*, Nucl. Phys. **A747**, 362 (2005).

[28] E. Epelbaum, H. Krebs, and U.-G. Meißner,, *Improved Chiral Nucleon-Nucleon Potential up to Next-to-Next-to-Next-to-Leading Order*, Eur. Phys. J. A **51**, 53 (2015).

[29] A. Ekström, G. Baardsen, C. Forssén, G. Hagen, M. Hjorth-Jensen, G. R. Jansen, R. Machleidt, W. Nazarewicz, T. Papenbrock, J. Sarich, and S. M. Wild, *Optimized Chiral Nucleon-Nucleon Interaction at Next-to-Next-to-Leading Order*, Phys. Rev. Lett. **110**, 192502 (2013).

[30] R. Navarro Perez, J. E. Amaro, and E. Ruiz Arriola, *Phenomenological High Precision Neutron-Proton Delta-Shell Potential*, Phys. Lett. B **724**, 138 (2013).

[31] R. Navarro Pérez, J. E. Amaro, and E. Ruiz Arriola, *Coarse-Grained Potential Analysis of Neutron-Proton and Proton-Proton Scattering below the Pion Production Threshold*, Phys. Rev. C **88**, 064002 (2013).

[32] R. Navarro Pérez, J. E. Amaro, and E. Ruiz Arriola, *Coarse-Grained NN Potential with Chiral Two-Pion Exchange*, Phys. Rev. C **89**, 024004 (2014).

[33] R. Navarro Pérez, J. E. Amaro, and E. Ruiz Arriola, *Statistical Error Analysis for Phenomenological Nucleon-Nucleon Potentials*, Phys. Rev. C **89**, 064006 (2014).

[34] R. Navarro Pérez, J. E. Amaro, and E. Ruiz Arriola, *Low-Energy Chiral Two-Pion Exchange Potential with Statistical Uncertainties*, Phys. Rev. C **91**, 054002 (2015).

[35] A. Ekström, B. D. Carlsson, K. A. Wendt, C. Forssén, M. Hjorth Jensen, R. Machleidt, and S. M. Wild, *Statistical Uncertainties of a Chiral Interaction at Next-to-Next-to Leading Order*, J. Phys. G **42**, 034003 (2015).

[36] R. Navarro Pérez, J. E. Amaro, and E. Ruiz Arriola, *Error Analysis of Nuclear Forces and Effective Interactions*, J. Phys. G **42**, 034013 (2015).

[37] P. Navrátil, V. G. Gueorguiev, J. P. Vary, W. E. Ormand, and A. Nogga, *Structure of $a = 10 - 13$ Nuclei with Two-Plus Three-Nucleon Interactions from Chiral Effective Field Theory*, Phys. Rev. Lett. **99**, 042501 (2007).

[38] H.-W. Hammer, A. Nogga, and A. Schwenk, *Colloquium: Three-Body Forces: From Cold Atoms to Nuclei*, Rev. Mod. Phys. **85**, 197 (2013).

[39] S. Weinberg, *Phenomenological Lagrangians*, Physica (Amsterdam) **96A**, 327 (1979).

[40] S. Weinberg, *Nuclear Forces from Chiral Lagrangians*, Phys. Lett. B **251**, 288 (1990).

[41] D. R. Entem, N. Kaiser, R. Machleidt, and Y. Nosyk, *Peripheral Nucleon-Nucleon Scattering at Fifth Order of Chiral Perturbation Theory*, Phys. Rev. C **91**, 014002 (2015).

[42] E. Epelbaum, H. Krebs, and U.-G. Meißner, *Precision Nucleon-Nucleon Potential at Fifth Order in the Chiral Expansion*, Phys. Rev. Lett. **115**, 122301 (2015).

[43] E. Epelbaum, A. Nogga, W. Glöckle, H. Kamada, U.-G. Meißner, and H. Witała, *Three-Nucleon Forces from Chiral Effective Field Theory*, Phys. Rev. C **66**, 064001 (2002).

[44] K. Hebeler, H. Krebs, E. Epelbaum, J. Golak, and R. Skibiński, *Efficient Calculation of Chiral Three-Nucleon Forces up to* N^3LO *for Ab Initio Studies*, Phys. Rev. C **91**, 044001 (2015).

[45] J. Liu, M. Mendenhall, A. Holley, H. Back, T. Bowles, L. Broussard, R. Carr, S. Clayton, S. Currie, B. Filippone *et al.* (UCNA Collaboration), *Determination of the Axial-Vector Weak Coupling Constant with Ultracold Neutrons*, Phys. Rev. Lett. **105**, 181803 (2010).

[46] P. J. Mohr, B. N. Taylor, and D. B. Newell, *CODATA Recommended Values of the Fundamental Physical Constants: 2010*, Rev. Mod. Phys. **84**, 1527 (2012).

[47] J. Beringer *et al.*, *Review of Particle Physics*, Phys. Rev. D **86**, 010001 (2012).

[48] G. J. M. Austen and J. J. de Swart, *Improved Coulomb Potential*, Phys. Rev. Lett. **50**, 2039 (1983).

[49] L. Durand, *Vacuum Polarization Effects in Proton-Proton Scattering*, Phys. Rev. **108**, 1597 (1957).

[50] V. G. J. Stoks and J. J. de Swart, *Magnetic Moment Interaction in Nucleon-Nucleon Phase-Shift Analyses*, Phys. Rev. C **42**, 1235 (1990).

[51] S. Weinberg, *Effective Chiral Lagrangians for Nucleon-Pion Interactions and Nuclear Forces*, Nucl. Phys. **B363**, 3 (1991).

[52] E. Epelbaum, *Few-Nucleon Forces and Systems in Chiral Effective Field Theory*, Prog. Part. Nucl. Phys. **57**, 654 (2006).

[53] C. Ordóñez, L. Ray, and U. van Kolck,, *Nucleon-Nucleon Potential from an Effective Chiral Lagrangian*, Phys. Rev. Lett. **72**, 1982 (1994).

[54] G. E. Brown, A. D. Jackson, and T. T. S. Kuo,, *Nucleon-Nucleon Potential and Minimal Relativity*, Nucl. Phys. **A133**, 481 (1969).

[55] A. Nogga, R. G. E. Timmermans, and U. van Kolck, *Renormalization of One-Pion Exchange and Power Counting*, Phys. Rev. C **72**, 054006 (2005).

[56] M. Pavón Valderrama and D. R. Phillips, *Power Counting of Contact-Range Currents in Effective Field Theory*, Phys. Rev. Lett. **114**, 082502 (2015).

[57] J. Bystricky, F. Lehar, and P. Winternitz,, *Formalism of Nucleon-Nucleon Elastic Scattering Experiments*, J. Phys. **39**, 1 (1978).

[58] P. La France and P. Winternitz, *Scattering Formalism for Nonidentical Spinor Particles*, J. Phys. **41**, 1391 (1980).

[59] H. P. Stapp, T. J. Ypsilantis, and N. Metropolis, *Phase-Shift Analysis of 310-MeV Proton-Proton Scattering Experiments*, Phys. Rev. **105**, 302 (1957).

[60] A. Gersten, *Electromagnetic Contributions to the Nucleon-Nucleon Interaction*, Nucl. Phys. **A290**, 445 (1977).

[61] C. M. Vincent and S. C. Phatak, *Accurate Momentum-Space Method for Scattering by Nuclear and Coulomb Potentials*, Phys. Rev. C **10**, 391 (1974).

[62] J. R. Bergervoet, P. C. van Campen, W. A. van der Sanden, and J. J. de Swart, *Phase Shift Analysis of 0–30 MeV pp Scattering Data*, Phys. Rev. C **38**, 15 (1988).

[63] F. Calogero, *Variable Phase Approach to Potential Scattering* (Academic Press, New York, 1967).

[64] K. Erkelenz, R. Alzetta, and K. Holinde,, *Momentum Space Calculations and Helicity Formalism in Nuclear Physics*, Nucl. Phys. **A176**, 413 (1971).

[65] K. A. Wendt, B. D. Carlsson, and A. Ekström,, *Uncertainty Quantification of the Pion-Nucleon Low-Energy Coupling Constants up to Fourth Order in Chiral Perturbation Theory*, arXiv:1410.0646.

[66] H. Krebs, A. Gasparyan, and E. Epelbaum, *Chiral Three-Nucleon Force at N4LO: Longest-Range Contributions*, Phys. Rev. C **85**, 054006 (2012).

[67] B. Tromborg, S. Waldenstrøm, and I. Øverbø, *Electromagnetic Corrections in Hadron Scattering, with Application to $\pi n \to \pi n$*, Helv. Phys. Acta **51**, 584 (1978).

[68] B. Tromborg and J. Hamilton, *Electromagnetic Corrections to Hadron-Hadron Scattering*, Nucl. Phys. **B76**, 483 (1974).

[69] B. Tromborg, S. Waldenstrøm, and I. Øverbø, *Electromagnetic Corrections to πn Scattering*, Phys. Rev. D **15**, 725 (1977).

[70] D. V. Bugg, *Coulomb Corrections to πn Elastic Scattering*, Nucl. Phys. **B58**, 397 (1973).

[71] H. A. Bethe, *Theory of the Effective Range in Nuclear Scattering*, Phys. Rev. **76**, 38 (1949).

[72] P. Navrátil, G. P. Kamuntavičius, and B. R. Barrett, *Few-Nucleon Systems in a Translationally Invariant Harmonic Oscillator Basis*, Phys. Rev. C **61**, 044001 (2000).

[73] G. P. Kamuntavičius, P. Navrátil, B. R. Barrett, G. Sapragonaite, and R. K. Kalinauskas, *Isoscalar Hamiltonians for Light Atomic Nuclei*, Phys. Rev. C **60**, 044304 (1999).

[74] J. L. Friar and J. W. Negele, *Theoretical and Experimental Determination of Nuclear Charge Distributions*, in *Advances in Nuclear Physics*, edited by M. Baranger and E. Vogt (Springer, New York, 1975), pp. 219–376.

[75] U. D. Jentschura, *Proton Radius, Darwin-Foldy Term and Radiative Corrections*, Eur. Phys. J. D **61**, 7 (2011).

[76] I. Angeli and K. P. Marinova, *Table of Experimental Nuclear Ground State Charge Radii: An Update*, At. Data Nucl. Data Tables **99**, 69 (2013).

[77] D. Gazit, S. Quaglioni, and P. Navrátil, *Three-Nucleon Low-Energy Constants from the Consistency of Interactions and Currents in Chiral Effective Field Theory*, Phys. Rev. Lett. **103**, 102502 (2009).

[78] Yu. A. Akulov and B. A. Mamyrin, *Half-Life and Value for the Bare Triton*, Phys. Lett. B **610**, 45 (2005).

[79] J. Dobaczewski, W. Nazarewicz, and P.-G. Reinhard, *Error Estimates of Theoretical Models: A Guide*, J. Phys. G **41**, 074001 (2014).

[80] G. A. Miller, B. M. K. Nefkens, and I. Ślaus, *Charge Symmetry, Quarks and Mesons*, Phys. Rep. **194**, 1 (1990).

[81] R. L. Workman, R. A. Arndt, W. J. Briscoe, M. W. Paris, and I. I. Strakovsky, *Parameterization Dependence of t-Matrix Poles and Eigenphases from a Fit to πn Elastic Scattering Data*, Phys. Rev. C **86**, 035202 (2012).

[82] A. Huber, Th. Udem, B. Gross, J. Reichert, M. Kourogi, K. Pachucki, M. Weitz, and T. W. Hänsch, *Hydrogen-Deuterium $1S-2S$ Isotope Shift and the Structure of the Deuteron*, Phys. Rev. Lett. **80**, 468 (1998).

[83] S. M. Wild, *Solving Derivative-Free Nonlinear Least Squares with Pounders*, Report No. ANL/MCS-P5120-0414, Argonne National Laboratory, 2014, http://www.mcs.anl.gov/publication/solving-derivative-free-nonlinear-least-squares-problems-pounders.

[84] T. Munson, J. Sarich, S. Wild, S. Benson, and L. C. McInnes, *TAO 2.0 Users Manual*, Technical Report No. ANL/MCS-TM-322 (Mathematics and Computer Science Division, Argonne National Laboratory, 2012), http://www.mcs.anl.gov/tao.

[85] M. Kortelainen, T. Lesinski, J. Moré, W. Nazarewicz, J. Sarich, N. Schunck, M. V. Stoitsov, and S. Wild, *Nuclear Energy Density Optimization*, Phys. Rev. C **82**, 024313 (2010).

[86] A. Ekström, G. R. Jansen, K. A. Wendt, G. Hagen, T. Papenbrock, B. D. Carlsson, C. Forssén, M. Hjorth-Jensen, P. Navrátil, and W. Nazarewicz, *Accurate Nuclear Radii and Binding Energies from a Chiral Interaction*, Phys. Rev. C **91**, 051301 (2015).

[87] I. Charpentier and J. Utke, Rapsodia: User Manual, Technical Report (Argonne National Laboratory), latest version available online at http://www.mcs.anl.gov/Rapsodia/userManual.pdf.

[88] M. I. Haftel and F. Tabakin, *Nuclear Saturation and the Smoothness of Nucleon-Nucleon Potentials*, Nucl. Phys. **A158**, 1 (1970).

[89] B. D. Carlsson, Licentiate thesis, Chalmers University of Technology, Gothenburg, Sweden, 2015, http://publications.lib.chalmers.se/publication/220844-making-predictions-using-eft.

[90] T. Mehen, I. W. Stewart, and M. B. Wise, *Wigner Symmetry in the Limit of Large Scattering Lengths*, Phys. Rev. Lett. **83**, 931 (1999).

[91] J. L. Friar, *Dimensional Power Counting in Nuclei*, Few-Body Syst. **22**, 161 (1997).

[92] See Supplemental Material at http://link.aps.org/supplemental/10.1103/PhysRevX.6.011019 for a tabulation of numerical values for LECs, statistical uncertainties, and covariance matrices.
[93] R. W. Hackenburg, *Neutron-Proton Effective Range Parameters and Zero-Energy Shape Dependence*, Phys. Rev. C **73**, 044002 (2006).
[94] S. Klarsfeld, J. Martorell, J. A. Oteo, M. Nishimura, and D. W. L. Sprung,, *Determination of the Deuteron Mean Square Radius*, Nucl. Phys. **A456**, 373 (1986).
[95] J. L. Friar, J. Martorell, and D. W. L. Sprung, *Nuclear Sizes and the Isotope Shift*, Phys. Rev. A **56**, 4579 (1997).
[96] M. Hoferichter, J. R. de Elvira, B. Kubis, and U.-G. Meißner, *High-Precision Determination of the Pion-Nucleon σ Term from Roy-Steiner Equations*, Phys. Rev. Lett. **115**, 092301 (2015).
[97] P. Lisowski, R. Shamu, G. Auchampaugh, N. King, M. Moore, G. Morgan, and T. Singleton, *Search for Resonance Structure in the np Total Cross Section below 800 MeV*, Phys. Rev. Lett. **49**, 255 (1982).
[98] S. I. Sukhoruchkin and Z. N. Soroko, *Atomic Mass and Nuclear Binding Energy for O-16 (Oxygen)*, in Nuclei with Z=1–54, Landolt-Börnstein—Group I Elementary Particles, Nuclei and Atoms, edited by H. Schopper (Springer, Berlin, Heidelberg, 2009), Vol. 22A, pp. 320–322.
[99] D. Stump, J. Pumplin, R. Brock, D. Casey, J. Huston, J. Kalk, H. L. Lai, and W. K. Tung, *Uncertainties of Predictions from Parton Distribution Functions. I. The Lagrange Multiplier Method*, Phys. Rev. D **65**, 014012 (2001).
[100] M. R. Schindler and D. R. Phillips, *Bayesian Methods for Parameter Estimation in Effective Field Theories*, Ann. Phys. (Amsterdam) **324**, 682 (2009).
[101] S. Habib, K. Heitmann, D. Higdon, C. Nakhleh, and B. Williams, *Cosmic Calibration: Constraints from the Matter Power Spectrum and the Cosmic Microwave Background*, Phys. Rev. D **76**, 083503 (2007).
[102] T. Holsclaw, U. Alam, B. Sansó, H. Lee, K. Heitmann, S. Habib, and D. Higdon, *NonParametric Dark Energy Reconstruction from Supernova Data*, Phys. Rev. Lett. **105**, 241302 (2010).